Nanomanufacturing and Metrology (2022) 5:209–229
https://doi.org/10.1007/s41871-022-00148-4

REVIEW PAPER

Indirect Measurement Methods for Quality and Process Control in Nanomanufacturing

Zhaoyan Fan[1] · Xiaochen Hu[1] · Robert X. Gao[2]

Received: 29 March 2022 / Revised: 1 August 2022 / Accepted: 1 August 2022 / Published online: 10 September 2022

Abstract
Rapid advancement over the past decades in nanomanufacturing has led to the realization of a broad range of nanostructures such as nanoparticles, nanotubes, and nanowires. The unique mechanical, chemical, and electrical properties of these nanostructures have made them increasingly desired as key components in industrial and commercial applications. As the geometric dimension of nano-manufactured products is on the sub-micron to nanometer scale, different mechanisms and effects are involved in the nanomanufacturing process as compared to those for macro-scale manufacturing. Although direct measurement methods using atomic force microscopy and electron beam microscopy can determine the dimensions of the nano structure with high accuracy, these methods are not suited for online process control and quality assurance. In comparison, indirect measurement methods analyze in-process parameters as the basis for inferring the dimensional variations in the nano products, thereby enabling online feedback for process control and quality assurance. This paper provides a comprehensive review of relevant indirect measurement methods, starting with their respective working principles, and subsequently discussing their characteristics and applications in terms of two different approaches: *data-based* and *physics-based* methods. Relevant mathematical and physics models for each of the methods are summarized, together with the associated effect of key process parameters on the quality of the final product. Based on the comprehensive literature conducted, it was found that: (1) indirect measurement, especially the data-based method, plays a critical role when it comes to online process control and quality assurance in nanomanufacturing, because of the short processing time compared to the direct method, and (2) physics-based method is providing a way to optimize the process set up for desired geometrical dimensions.

Keywords Measurement · Modeling · Nanomanufacturing · Quality control

1 Introduction

Nanomanufacturing, in the last decades, has rapidly evolved with the development of material, control, and manufacturing sciences. Recent research regards the study of nanomanufacturing as falling into two categories [1]: (1) The dimensions of the components are at the nanometric or micrometric scale with nanometric scale feature size, and (2) the geometrical accuracy of the components is at the nanometric scale.

For the first category, research has shown that when the scale of specific components reaches the nanometric scale, the performance of components is greatly improved [2]. For example, the nanoparticles of metal material can improve light absorptivity when the particle dimensions match the light wavelength [3]. The superparamagnetic effects associated with nano-ferromagnetic particles improve magnet stability at low temperatures [4]. Additionally, carbon nanotubes enhance the characteristics of polymeric matrices by increasing their tensile and shear stiffness 23-fold [5]. In addition to nanoparticles and tubes, other nanomanufacturing products are also widely studied for industrial applications, including nanofilms and nanotubes for sensing elements [6–11], thermal energy harvesting [12], flame retardants [13], self-cleaning mechanisms [14, 15], polymers [16] and nanowires for energy saving [17, 18], and structural reinforcement [19, 20].

✉ Zhaoyan Fan
zhaoyan.fan@oregonstate.edu

[1] School of Mechanical, Industrial, and Manufacturing Engineering, Oregon State University, Corvallis, OR 97331, USA

[2] Department of Mechanical and Aerospace Engineering, Case Western Reserve University, Cleveland, OH 44106, USA

The second category refers to processes for producing products of high-dimensional tolerances, e.g., diamond machining of metals and ultrasonic-assisted machining, which enables the advanced stability and surface quality of the products [21, 22]. The scope of this paper mainly addresses the measurement methods for the first category of nanomanufacturing. Depending on the type of nanostructures and their applications, the parameters of interest for the nanomanufacturing products cover a wide spectrum. According to the physical nature of these parameters, they can be categorized into three major types:

- Critical dimensions (CDs), also considered geometrical properties, are the geometric dimensions determining the overall performance of the products. Depending on the type of nanostructure being produced, CDs cover the structural length, width, thickness, roughness, and angle of the geometric features [23].
- Mechanical properties mainly include Young's modulus, hardness, and other material-related characteristics for the structures on the nanoscale.
- Thermal properties consider the heat capacity and conductivity of nanowires and nanoparticles.

Compared to the macroscale manufacturing processes, determining properties in nanomanufacturing faces new metrological challenges due to the scale of nanoproducts being close to or even smaller than the wavelength of light, e.g., ranging from 100 to 1000 nm. On the other hand, measurement technologies developed over the past decades can be categorized into two groups: direct and indirect methods, as shown in Fig. 1. The direct methods obtain these properties through direct imaging of the nanostructure or measurement process using atomic force microscopy (AFM) [24–26], scanning electron microscopy (SEM) [27], photoinduced force microscopy (PiFM) [28], electrostatic force microscopy (EFM) [29], scanning transmission electron microscopy (STEM) [30–32], optical scatterometry (OSM) [33–35], X-ray imaging [36–40], and other hybrid methods [41–45]. Because of the capability of obtaining CDs through direct optical or physical interaction, the direct measurement methods can achieve a high measurement resolution of up to 0.1 nm.

In addition to serving as a metrological approach, direct methods are also used to calibrate each other or validate other measurement methods. At the same time, direct methods are also subject to constraints due to the direct physical interaction between the probes or electron/light beams and the nanostructure being measured. Measuring CDs on the nanometer scale requires a high spatial resolution on the level of at least a sub-nanometer. This measurement would need to define small incremental steps to move the probe along the horizontal trajectories on the scanned surface (e.g., AFM, PiFM, and EFM) or apply high spatial resolution to the light detectors (e.g., SEM, OSM, STEM, and X-ray imaging). Considering the overall dimensions of the nanoproducts and the large amount produced by nanomanufacturing, applying such high-resolution scanning would result in a long measurement period. As an example, AFM scans 1 mm^2 in 1200 s [46]. Therefore, the direct methods are generally used for offline sampling and are not intended for in-process monitoring.

In comparison, indirect measurement quantifies in-process parameters, such as temperature [47], pressure [48], and etching solution concentration [49, 50], during the nanomanufacturing processes. Through proper data analytical techniques, these parameters are interpreted to infer the CDs and various mechanical and thermal properties by

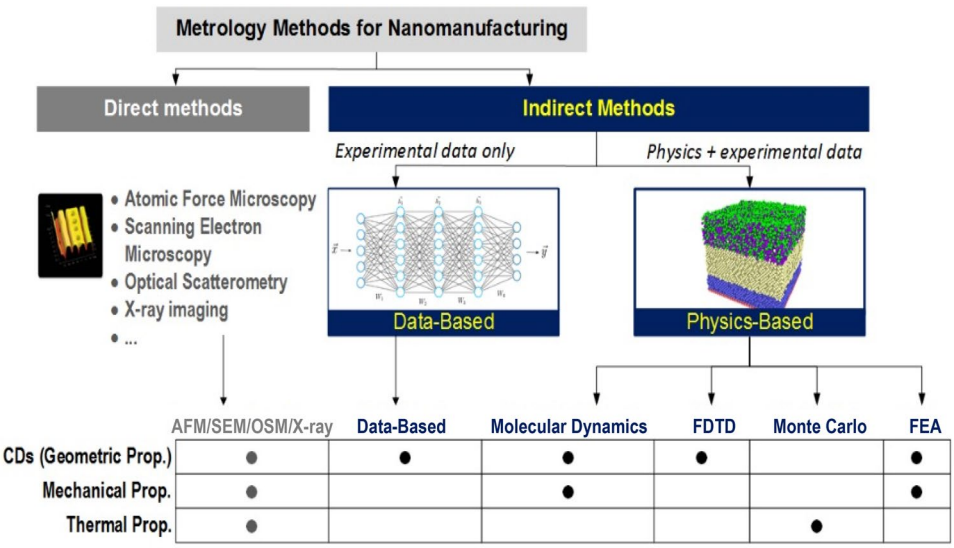

Fig. 1 Indirect nanoscale measurement methods (*FDTD* finite difference time domain method, *FEA* finite element analysis method)

referring to the physics of the underlying process and/or the historical data [51]. Because these parameters are measured in real time, they can be used as feedback to adjust the operation without stopping the process [52]. As an example, an indirect measurement technique using deposition time, fluid atom concentration, temperature, and electric field intensity to infer the thickness and surface roughness of a nanofilm has a reported sampling rate of up to 10 samples/s, making online monitoring of the nanofilm manufacturing process feasible [53].

The core challenge in indirect methods is to establish the relationship between the measurable parameters and the properties of the produced nanostructures. This relationship justifies the meaningfulness and effectiveness of an in-process measurement. As illustrated in Fig. 1, this paper categorizes the indirect measurement methods into two major classes: *data-based* and *physics-based* methods. The former method establishes the relationship between in-process parameters and properties of the nanostructures through machine learning algorithms, which do not involve physical models and may be considered a black box. As the data-based method relies on much data to train the model, it is mainly adopted for measuring the CDs of the nanostructure, which can be accessed by direct methods. The latter method, in comparison, depends on the underlying physics of the manufacturing process to establish the process–property correlation. According to the mathematical models being applied to the physical dynamics and chemical reactions, the physics-based methods developed in the literature can be divided into four major categories: molecular dynamics (MD) simulations, the finite difference time domain (FDTD) method, the Monte Carlo (MC) method, and finite element analysis (FEA). As these models can simulate material behavior in macro- or microscales, the physics-based method can extend the scope beyond the measurement of CDs, for instance, to predict the mechanical and thermal properties of the nanoproduct.

This paper systematically reviews the indirect measurement methods and associated models and algorithms, focusing on the measurement principles and applications. Specifically, in the category of physics-based methods, four primary techniques that have been extensively investigated are discussed: MD, FDTD, MC, and FEA methods. The remaining paper is organized as follows: Sect. Data-based Methods discusses the data-based method and the associated mathematical algorithms. In Sect. Physics-based Methods, indirect measurement techniques based on physical principles are introduced, including MD simulations, the FDTD method, the MC method, and the finite element method. For each method, representative applications are introduced. Discussion of the presented work is presented in Sect. Discussion. In Sect. Conclusion, conclusions and future research directions are summarized.

2 Data-Based Methods

The data-based method is rooted in statistical modeling to build a relationship between input and output parameters. The rapid development of machine learning techniques has made data-based modeling increasingly applicable to estimating the properties of nanostructures.

2.1 In-Process Parameters in the Nanomanufacturing Techniques

According to how a nanostructure is fabricated, nanomanufacturing processes can be classified as "top-down" or "bottom-up" approaches, as shown in Fig. 2. The associated process variables in these approaches are listed in Table 1. In the top-down approach, the material is subtracted from the raw piece, which includes nanomachining, etching, and nanolithography. Their manufacturing processes are related to different process parameters. Nanomachining is defined as the material removal process in which a dimension accuracy of 100 nm or better, even toward the 1-nm level, can be achieved [5]. The common nanomachining includes cutting, grinding, polishing, and single-point diamond turning. The

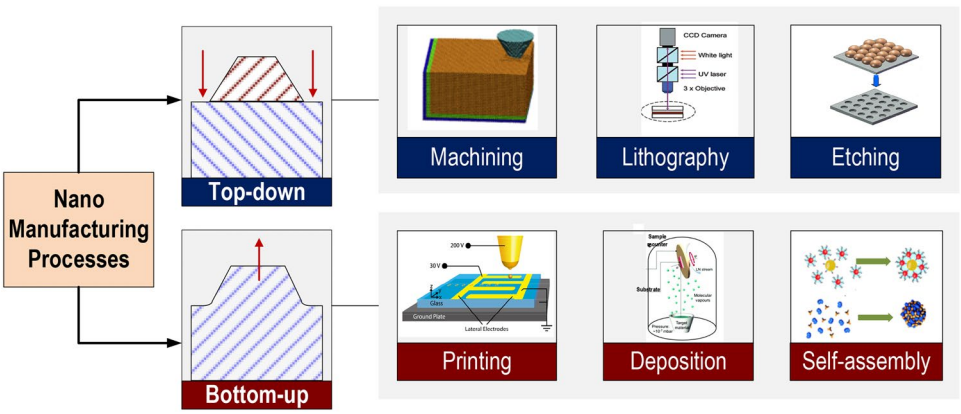

Fig. 2 Nanomanufacturing techniques

Table 1 Nanomanufacturing approaches and process variables

Approaches	Techniques	Process variables
"Top-down"	Cutting	Cutting speed, cutting depth, and feed rate [54, 55]
	Etching	Etching time, solution concentration, and catalyst [50, 59]
	Nanolithography	Aperture shape, photoresist, and mask material [53, 56]
"Bottom-up"	Self-assembly	Solution concentration, temperature, time, and evaporation rate [47, 152]
	Chemical synthesis	Particle-to-solution ratio [153, 149]

cutting parameters, such as cutting speed, cutting depth, and cutting rate, influence the CDs of manufactured components as the macroscale machining techniques. Etching is a type of chemical material removal technique. The patterns obtained by etching depend on the etching time, temperature, solution concentration, etc. Nanolithography applies an electron beam or light beam to etch, write, and print raw material and then obtain nanoscale components. The main parameters related to the nanolithography process include layer material, layer thickness, aperture shape, and light wavelength.

In the bottom-up approach, the nanostructures are built from molecules or particles through mechanical assembly or chemical synthesis. The common bottom-up methods include nanoprinting, deposition, and self-assembly. In-process parameters, such as vapor pressure in deposition, solution viscosity, and injection velocity in printing, influence the performances of manufactured components for each bottom-up approach.

2.2 Effect of In-process Parameters on Nanostructure Properties

The relationship between the in-process parameters and nanostructure properties has been quantitatively studied in recent decades. Keong et al. studied the nanoscale cutting process for aluminum 7075 and found that the surface roughness of the product increases with the cutting depth [54]. Zhang [55] used elliptical vibration cutting as an amplitude compensation method to achieve ultra-precise nanostructure fabrication. Sreemanth et al. [56] found that the scanning speed in optical nanolithography determines the width and depth of etched line structures. Piner et al. [57] found that the width of nanolines by dip-pen nanolithography is sensitive to the scanning speed of the pen-tip and the transport rate of the solution from the tip to the substrate. An increased scanning speed and a few traces resulted in a decreased line width. Ahn et al. [47] found that the orientation of nanoparticle patterns depended on the applied magnetic field distribution in high-resolution magnetic printing. Wilson et al. [58] measured the grain size of inkjet-printed polymer films under different solution concentrations. Kazuya et al. [50] used wet etching to form nanoholes in different concentration solutions containing HF and H_2O_2 with silver nanoparticle catalysts. The shape of the silver particles was an essential factor in determining the direction of nanoholes, while the etching time and solution concentration determined the length and diameter of the nanoholes.

Yuki et al. [59] studied the influence factors on silicon nanowires formed by catalytic chemical etching in Ag_2O/HF solution. This work found that solution concentration, etching time, and temperature can influence the length of the nanowires, as shown in Fig. 3. Zhao et al. [60] found that the microstructure and morphology of Ag catalyst film affect the silicon nanowire fabrication process in chemical etching.

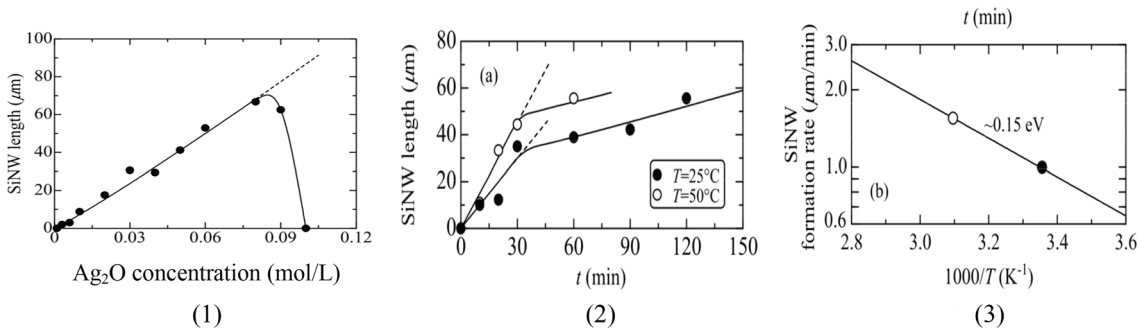

Fig. 3 Factors affecting Si nanowire formation in catalytic chemical etching. **1** Nanowire length vs. Ag_2O concentration at 25 °C for 30 min. **2** Nanowire length versus etching time in Ag_2O/HF solution at 25 and 50 °C. **3** Nanowire formation rate versus reciprocal solution temperature [59]

Xie et al. [61] fabricated a well-ordered silicon nanowire array using an Ag-assisted chemical etching technique and found a linear relationship between the length of the nanowire and the etching time.

2.3 Data-Based Model in Nanomanufacturing

From experimental results in nanomanufacturing, a certain relationship is shown to hold between in-process parameters and properties of nanoscale products. Data-based modeling trained by the historically sampled data from experiments can describe this relationship based on experimental approaches, particularly for complicated processes or nanostructures where the physical relationship is difficult to obtain through theories [62, 63].

Typical machine learning algorithms for building data-based models were summarized in [64]. According to the requirement on ground truth data (labeled data), machine learning algorithms are classified into three major categories: supervised, unsupervised, and reinforcement learning. Supervised learning takes the labeled data as the output of the model and correlates some of them with the process variables (input) for model training. The remaining labeled data are used to validate and test the trained models. Random forest (RF), support vector machine (SVM), decision tree, and Naïve Bayes are typical supervised learning algorithms [64]. In comparison, unsupervised learning algorithms do not require labeled data but only rely on the process variables. Typical unsupervised learning includes clustering, principal component analysis, and singular value decomposition. Compared with supervised learning, unsupervised learning does not require data labeling [64], which may take a significant amount of time and effort to establish the ground truth. Reinforcement learning is a relatively new category in machine learning that determines a data-based model through an iterative approach. In each iteration, reinforcement learning statistically adjusts the model parameters by referring to the "rewards" representing the estimation/prediction accuracy. Through this approach, the algorithm seeks an optimal solution for long-term and maximum overall rewards. Compared with the other two categories of machine learning methods, the architecture of reinforcement learning algorithms generally has a higher level of complexity and requires a larger amount of process variable data for model training. In applications, labeled data are optional for reinforcement learning. Typical reinforcement learning methods are realized by a deep neural network, recurrent neural network, deep belief network, etc. [64].

In recent years, machine learning methods have been applied to nanostructures [65–72], nanobiomedication [73, 74], nanoidentification [75], and nanomaterials [66]. Specifically, for nanomanufacturing, supervised and unsupervised learning methods have been widely applied to building data-based models for data analysis in indirect measurements. Table 2 lists the reported modeling algorithms together with the parameters and estimated CDs found in recent publications.

Hou et al. [63] studied a data-based model for the nanoparticle wet milling process. The model was trained through the *response surface method* (RSM) to represent the relationship between the milled grain size and process parameters such as milling time and rotation velocity. The model was further optimized by the genetic algorithm to minimize the estimation error. Erdemir et al. [76] studied the effect of milling parameters on nanoparticle size during a high-energy ball milling process based on the RSM. A central composite design was implemented to determine the effects of milling parameters, i.e., milling time, the ball-to-powder ratio, and milling speed, on the produced nanoparticle diameter. Yordem et al. [51] studied the effect of the in-process parameters of electrospinning on polyacrylonitrile nanofiber diameter. The RSM was used to design the experiments at the setting of solution concentration, voltage, and collector distance. Ayu et al. [49] developed an RSM model to study the influence of metal-assisted chemical etching process variables on the nanopillar profiles. The process variables include solution and catalyst concentration, deposition time, and etching time. Experimental validation showed an estimated error of 1.8% by referring to the dimensions measured via SEM.

Research [77] studied the behavior of bias power and Cl_2 concentration in silicon trench etching and their influence on the etching rate and the variations in sidewall profile. Huey et al. [78] built the RSM and artificial neural network models

Table 2 Statistical models for estimating CDs of nanostructure

Modeling methods	Measured parameters	Estimated critical dimension	Measurement error
Response surface method	Speed, molecular weight, temperature, duration, solution, solution concentration, etc.	Grain size, surface roughness, profile angle	0.2%–2% [48, 77, 78, 149–151]
Artificial neural network	Speed, molecular weight, temperature, duration, solution, solution concentration, etc.	Surface roughness	Less than 5% [78]
Support vector machine	Voltage and anodization time	Layer thickness	18%–26% [154]

for the chemical etching process to correlate the etching variables, including etching temperature, etching duration, and solution concentration, with the surface roughness of the etched surfaces. The model shows that for individual process parameters, the relationship between the parameter and product surface roughness varies significantly for different materials. Compared to the experimental results, the estimated roughness achieves an accuracy of 95%. Lin et al. applied the SVM to correct errors in microscope photographs when evaluating nanostructure thickness [79]. Kim tested eight machine learning methods to estimate the thickness of TiO_2 films. A comparative study of these methods with respect to the estimation accuracy has revealed that the decision tree algorithm achieved the highest accuracy of 82%, while K-nearest neighbor learning had the lowest accuracy of 70%. Du et al. estimated the mobility of aluminum atoms on Al_2O_3 nanofilm during ductile deformation based on the SVM with an accuracy of 69%–82% [80]. Notably, most of the algorithms in the literature used to build data-based models are of the supervised or unsupervised learning type. Broad-based applications of reinforcement learning for indirect measurement are yet to be seen.

Data-based models can be applied to nonlinear and complex systems at the cost of requiring a certain amount of historical data to train the models. Compared with the physics-based method, the data-based method is advanced in the short response time for a trained model to estimate CDs from the measured process variables. As data-based models entirely depend on the training data, the developed data-based model can hardly be extended to other applications with different model architectures, manufacturing platforms, or materials [81].

3 Physics-Based Methods

3.1 Molecular Dynamics

Nanomanufacturing occurs at the molecular level by manipulating materials at the atomic and molecular scales. Physics-based modeling methods are generally based on the well-understood physical or chemical dynamics of the specific nanomanufacturing processes. The particle behavior in the nanomanufacturing process can be understood from theoretical analysis, and the results of the theoretical analysis can be calculated through numerical simulation. On the basis of the analysis scale and the type of properties studied, four physics-based modeling techniques will be discussed to obtain the properties of nanoscale products with respect to their principles and application status.

MD modeling is a method that determines the motion of a group of molecules following Newton's second law, correlating the movement and the force applied together. The force field that results in the movements can be calculated based on the initial positions of the molecules and their interaction with neighboring molecules. In the MD analysis, the molecular motion in each set time step can be simulated based on the theories, making the process transparent. This advantage makes it a good complement for experiments, visualizing the motion of molecules to study the mechanisms of the nanomanufacturing process from the microscopic perspective. As the MD method solves the trajectory of each molecule, it simulates the actual nanomanufacturing process with high spatial accuracy.

3.1.1 MD Principles

3.1.1.1 Force Field As the force field determines the motion of molecules physically, modeling the force field is one of the keys to the MD method. The study of a force field for describing microscopic particle motion was started in the 1960s by Aligner's group [82] to calculate the motion of hydrocarbon molecules. Thus far, the concept has been extended to study various types of particles, such as peptides [83], aluminum [84], germanium [85], and ethane [86]. In general, the force field resulting in the potential energy of a *single molecule* in the MD model can be expressed as given in Eq. (1) [87].

$$V = V_{\text{bond}} + V_{\text{angle}} + V_{\text{torsion}} + V_{\text{oop}} + V_{\text{nonbond}} \tag{1}$$

where V_{bond} is the energy change related to bond length variation in a molecule, as shown in Fig. 4 (1), where the solid lines/circles show the molecule at the equilibrium position, while shapes in dash lines/curves show the positions after the conditions changed; V_{angle} is the energy change related to bond angle change, as shown in Fig. 4 (2); V_{torsion} is the energy change when a certain torsion is applied to the

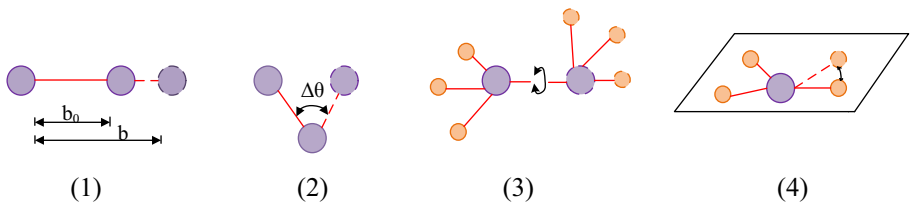

Fig. 4 Molecular movement model. **1** Translation of molecule. **2** Rotation of molecule. **3** Torsion of molecule. **4** "Out-of-plane" motion

molecule, resulting in a rotation, as shown in Fig. 4 (3); V_{oop} is the "out-of-plane" energy, representing the energy change when one part of the molecule is moving out of the plane, as shown in Fig. 4 (4); $V_{non\text{-}bond}$ is the noncovalent interaction energy, including van der Waals interactions and Coulombic interactions.

According to the physics of each component, Eq. (1) can be extended as [82, 87]:

$$V(r) = \sum_{bonds} \frac{k_b}{2}(b-b_0)^2 + \sum_{angles} \frac{k_\theta}{2}(\theta-\theta_0)^2 + \sum_{torsions} \frac{k_\phi}{2}[\cos(n\phi+\delta)+1] + \sum_{oop} \frac{k_\psi}{2}(\psi-\psi_0)^2 + \sum_{\substack{nonbond\\pairs}} 4\varepsilon_{ij}[(\frac{\sigma_{ij}}{r_{ij}})^{12} + (\frac{\sigma_{ij}}{r_{ij}})^6] + \frac{q_i q_j}{r_{ij}} \quad (2)$$

where $k_b, k_\theta, k_\phi, k_\psi$ are the stiffness coefficient of the bond length, angle, torsion, and out-of-plane motion, respectively; b is the distance between atoms, b_0 is the equilibrium distance; θ is the angle between two bond vectors, θ_0 is the equilibrium angle; ϕ is the torsion angle, δ is the phase, n is the dihedral potential, ψ is the out-of-plane displacement, and ψ_0 is the equilibrium displacement. The last summation term of Eq. 2 represents the van der Waals interaction, composed of a 12–6 Lennard–Jones potential and Coulombic interaction. In this term, σ_{ij} is the size parameter of atom i and atom j,ε_{ij} is the energy parameter, r_{ij} is the distance between atoms i and j [88], and q_i and q_j are the effective charges on atom i and atom j, respectively.

Based on the application and the type of molecules, the detailed parameters measured or approximated can be substituted into the force field formation equations (Eqs. 1 ~ 2) to generate different force field models. Examples of these models include the first force field developed by Allinger's group, MM2 [89], MM3 [90], and MM4 [91], which are used to study hydrocarbons. The force field concept has been further extended in recent decades to study complex systems with large molecules in nanomanufacturing. Dreiding and universal force fields are two examples that can be used to model all molecules [92]. AMBER [93] is a force field model that can be applied to biomolecules, canonical/noncanonical nucleic acids, and proteins in water. The CHARMM force field [94] studies small and large biological macromolecules, such as lipids and carbohydrates [82]. GROMOS [95] was developed to simulate condensed matter.

In addition, other types of force field models, such as OPLS [96], COMPASS [97], CFF [98], and MMFF [99], have been developed to describe the behavior of specific molecules or particles. The application scope of every force field is introduced in [82]. The performance of a force field strongly depends on the system and particle type being simulated. Each force field has its strengths and weakness related to the molecular formation procedure and environment, while some general force field models can generate reasonable results comparable with experimental results for a wide range of molecules and various environments [100].

3.1.1.2 Motion Algorithm The force field model in Eqs. 1–2 is applied to each molecule in a material, and the motion of each molecule can be described by a second-order partial derivative function based on Newton's second law [92]:

$$m_i \frac{d^2 r_i}{dt^2} = f_i = -\frac{\partial}{\partial r_i} V(r_1, r_2, ..., r_N) \quad (3)$$

where m_i and r_i are the mass and location of atom i, respectively, and $V(r_1, r_2, ..., r_N)$ is the sum of the potential energy of atoms 1–N in their initial locations.

The molecular trajectories are calculated in n consecutive time steps, t_0, $t_0+\Delta t$, …, $t_0+n\Delta t$. In each discrete time step, a solution to the second-order partial differential equation, Eq. (3), is obtained through numerical methods. The most used numerical method includes the Verlet integrator (leap-frog algorithm) and velocity-Verlet algorithm. In the Verlet integrator method, the solution is obtained through iterative approximations, expressed as [101]:

$$\begin{cases} r_i(t_0+\Delta t) = r_i(t_0) + v_i(t_0+\frac{\Delta t}{2})\Delta t \\ v_i(t_0+\frac{\Delta t}{2}) = v_i(t_0-\frac{\Delta t}{2}) + a_i(t_0)\Delta t \end{cases} \quad (4)$$

where v_i and a_i represent the velocity and acceleration of the molecule in the studied space, respectively. The velocity-Verlet algorithm further considers the second-order integration of acceleration in calculating the molecule's position and accordingly solves Eq. (3) as follows:

$$\begin{cases} r_i(t_0+\Delta t) = r_i(t_0) + v_i(t_0)\Delta t + \frac{1}{2}a_i(t_0)\Delta t^2 \\ v_i(t_0+\Delta t) = v_i(t_0) + \frac{1}{2}[a_i(t_0) + a_i(t_0+\Delta t)]\Delta t \end{cases} \quad (5)$$

In addition, other methods, such as the Euler method [102] and the Crank–Nicolson method [103], are also reported in the MD modeling research for nanomanufacturing. Although complicated algorithms that include more terms in the expression for the molecule trajectory will improve the accuracy of the model, considering the many molecules within a nanostructure, such algorithms generally result in an increased computational load [104, 105]. In practical applications, selecting numerical algorithms for solving the trajectory in the MD method

generally considers the balance between accuracy and computational efficiency.

3.1.2 MD Applied to Nanomanufacturing

3.1.2.1 Mechanical Properties The MD method has been applied to simulating nanoscale components from which mechanical properties are derived. The effectiveness of the method has been verified experimentally, as reported in the literature. Tang et al. applied transmission electron microscopy (TEM) and MD simulations to study the deformation and fracture mechanism of Si nanowires with a diameter of 9 nm [106]. The nanostructure behavior under tensile and bending loads was obtained through MD simulations and experiments, as shown in Figs. 5 and 6. In the tensile test (Fig. 5), the nanowire breaking process during increasing normal stretch stress on the two ends of the nanowire was simulated. The simulated linear relationship (approximate) between stress and strain well matches the experimental results. Figure 6 shows the observed nanowire deformation during the bending test. The nanowire was imaged by TEM in the experiments when the bending moment was loaded to the nanowire. A crack was visually observed on the image when the bending strain exceeded 21.5%. This result matches well with the MD modeling results, as shown in Fig. 6 (2) [106].

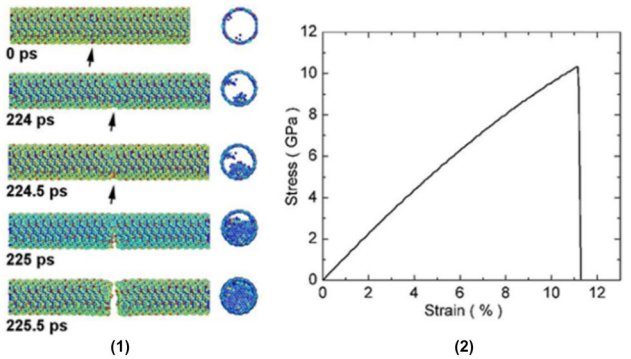

Fig. 5 Simulated nanowires under tensile test. **1** Simulated nanowire structure in the side view and cross-sectional view. **2** Simulated stress–strain relationship [106]

Li et al. simulated physical vapor deposition and the nanoindentation process by MD to study the hardness and defect of nanofilm under different deposition temperatures [107]. A piece of Cu/Au thin film of $7.2 \times 7.2 \times 30$ nm^3 was simulated in the study. An ideal spherical indenter with a radius of 2 nm at a constant velocity of 50 m/s was built to simulate the nanoindentation process by indenting the depth from 1.6 nm to 2.2 nm. The force–depth curve was calculated during the indentation process [107]. Li et al. studied via the MD method the process in which the nanofilm thickness changes the glass transition temperature, Young's modulus, and yield stress [86]. Lai et al. conducted a 3D MD simulation to study the nanometric cutting of germanium, as shown in Fig. 7. The studied workpiece dimension was set as $45 \times 27 \times 12$ nm^3. The uncut thickness and cutting force with different cutting depths on different crystal orientation faces were calculated based on this MD model. This work can provide references for selecting the cutting parameters and modeling the nanometric cutting mechanisms [85].

3.1.2.2 Critical dimensions Chen et al. built a kinetic competition model with kinetic parameters from in situ TEM to estimate the diameter of silicon nanowire [108]. Sindhu et al. studied nanoparticle formation in an inter-gas evaporation technique, and the particle size and distributions were predicted by solving the general dynamic equations through the nodal approach under different ambient conditions. When the injecting energy is higher than the vaporization energy,

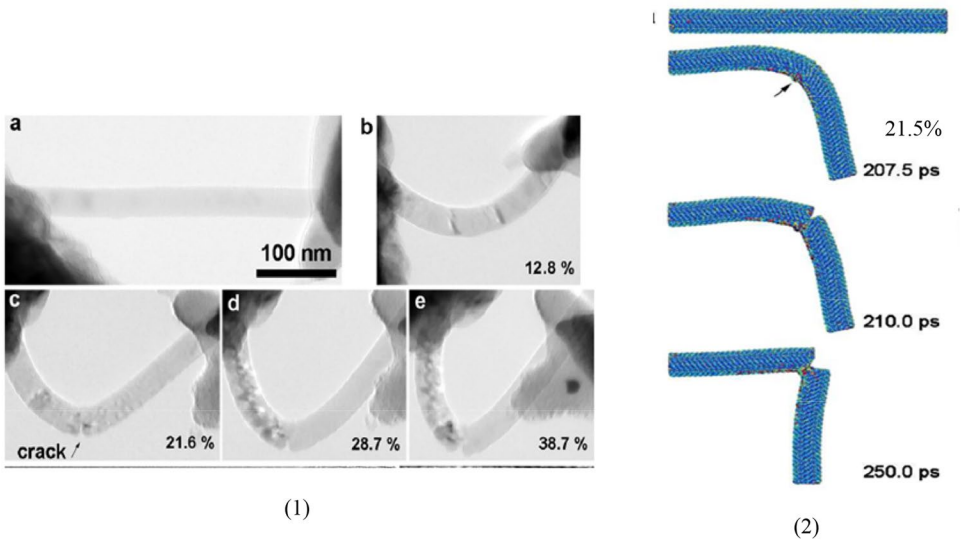

Fig. 6 Comparison of nanowire behavior in the bending test under experiments and simulation. **1** Experimental image obtained via TEM. **2** Simulated nanowire [106]

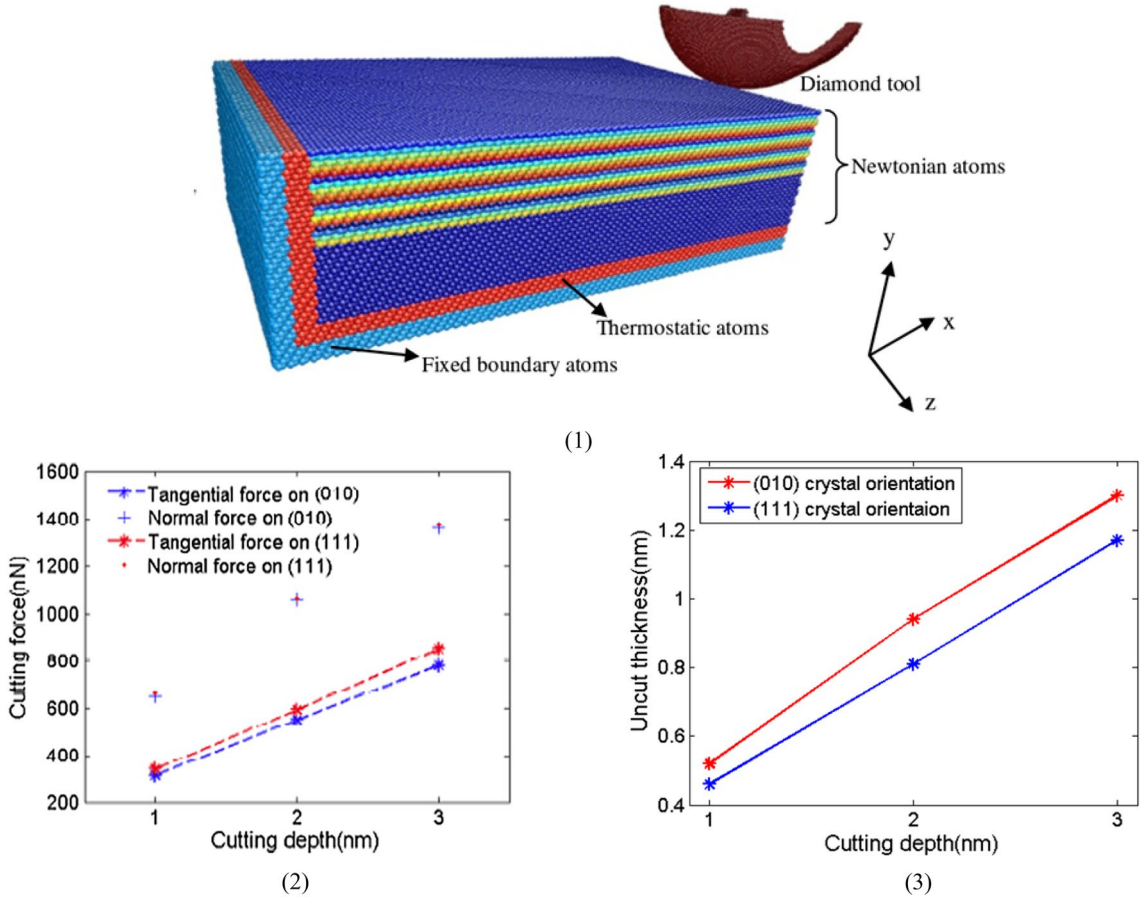

Fig. 7 Simulated nanometric cutting process **1** MD simulation model. **2** Simulated uncut thickness at different cutting depths on the (010) and (111) crystal orientation face. **3** Simulated cutting force at different cutting depths [85]

the dimensions of the produced particles are reduced [109]. Xu et al. studied the supramolecular structure of surfactant and carbon nanotube aggregates in aqueous solution using atomic-level MD simulation [110]. The surfactant adsorption on a nanotube with a hemimicellar structure was found to be consistent with the observations under TEM in the structure periodicity (4.5 ± 0.5 nm). The average height of the hemimicelle is also in good agreement with the experimentally measured height [110]. The MD method was also applied to simulate the deposition and annealing of a Ni–Al wire on a Ni substrate [84]. Sputtering parameters (including the incident energy, incident angle, and substrate temperature) and subsequent heat treatment were considered in the model.

The MD method has a wide application in analyzing the nanomanufacturing process and estimating the mechanical properties of nanoscale products from the initial and in-process working conditions. The MD method can build a relationship between the in-process parameters and nanoscale product. It can also predict the mechanical properties of nanoscale products. However, as the simulated elements are generally at the molecular dimension level, modeling the nanostructure generally includes many elements. In addition, since the MD needs to be sampled every 10–100 fs, simulating the transients of the nanomanufacturing process requires at least trillions of time steps, which further increases the computational load [82]. In general, on the current computation platforms, such a constraint limits the MD method to simulating processes shorter than a few seconds.

3.2 Finite Difference Time Domain Method

The FDTD method is a numerical method for modeling an electromagnetic field and its propagation in 1D, 2D, or 3D space. The idea of FDTD was first developed by Yee [111] in the 1960s. The technique was fully developed by Umashankar and Taflove in the 1970s [112]. Since then, the FDTD method has become a fundamental tool for studying microwaves and optics [113]. In recent decades, the FDTD method has been used to model the optical properties of nanostructures [114] and the nanomanufacturing process, such as nanolithography [115] and surface plasmon

polarization processes [116]. In these processes, the light waves or photons dynamically interact with the molecules of the photosensitive material, change the material characteristics, and determine the nanostructure CDs in consecutive procedures. To mathematically model the electromagnetic waves, the FDTD method discretizes the space and time to calculate a time-varying electromagnetic field in each time step based on Faraday's law and Ampere's law [117].

In nanomanufacturing, FDTD has been used to determine the relationship between the applied light intensity and the geometry/shape of the nanostructure. Shao et al. built a two-dimensional FDTD model to study fabricating high-density arbitrary patterns on a sub-100-nm scale in the ultraviolet nanolithography process, as shown in Fig. 8 [113]. Figure 8 (1) shows the modeled setup, with UV light applied to react with the photoresist film under the metal mask. Simulation results from the FDTD model are compared with the theoretical results (analytical) in Fig. 8 (2), where a good matching between the two types of data is observed. The model was also used to simulate the electric field distribution in the photoresist layer, as shown in Fig. 8 (3). When the aperture in the metal mask is reduced from 50 to 20 nm, the light transmission is significantly reduced to 60%. This relationship provides a reference for manufacturers to determine the aperture size and light source intensity according to the preferred nanostructure CDs.

In the work presented by Wang et al. [118], the FDTD method was used to simulate an electric field distribution through square, rectangular, and bowtie apertures. As shown in Fig. 9 [118], the simulation results were consistent with experimental data. Chang et al. applied an FDTD simulation to obtain the morphology at different penetration depths in the photoresist film during 3D nanolithography, as shown in Fig. 10 (1) [119]. Consistent morphologies were observed by comparing the simulation results and the SEM image at penetration depths from 40 to 650 nm, as shown in Fig. 10 (2). The FDTD simulation results were used to predict the CDs of nanostructure produced by nanolithography [119].

Kim et al. developed a simulation code, AMADEUS (advanced modeling and design environment for sputter process), to simulate the topography in ion beam-induced nanofabrication based on the ion beam milling process. The ion beam milling hole depth and diameter were predicted [120]. Dragos et al. analyzed nanosphere lithography progress and the relationship between nanosphere shapes and

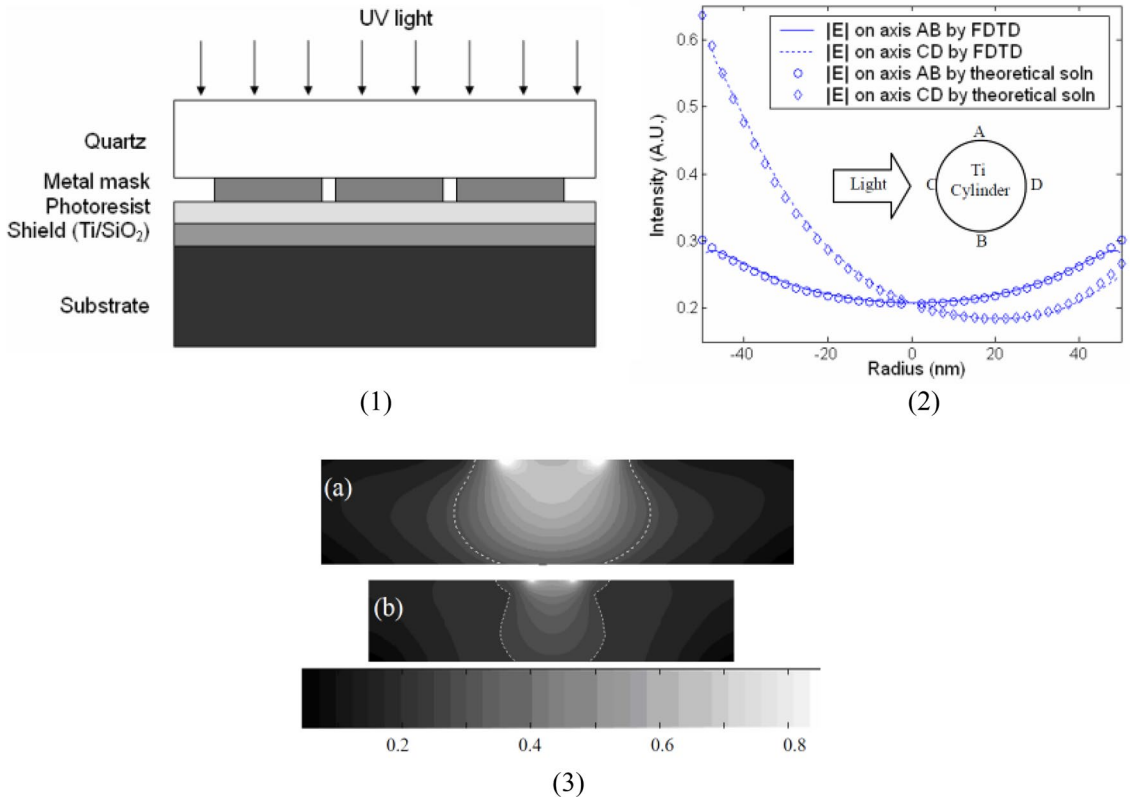

Fig. 8 Photolithography modeled using the FDTD method to study the effect of aperture size on the nanostructure CDs. **1** Schematic view of the photolithography process. **2** Comparison of the electric field distribution of the FDTD simulation and theoretical solution. **3** Electric field distribution in the photoresist with (a) 50-nm aperture and 60-nm resist thickness (b) 20-nm aperture and 50-nm resist thickness [113]

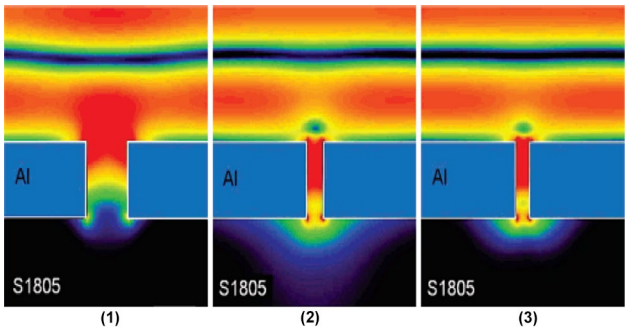

Fig. 9 Electric field distribution with different apertures. **1** Square, **2** rectangular, **3** bowtie [118]

electric fields in photolithography. A shape-prediction model was built based on the FDTD method [121]. Sreemanth et al. studied the influence of laser scanning speed on the width of nanolines [56]. FDTD was used to numerically design the bowtie apertures to estimate the nanoline width under a scan speed of 0.2 to 0.9 μm/s with an error of 21% [56]. Mishra and Palai presented a technique for measuring the intensity of reflection, transition, and absorbed light to compute the percentage of porosity in porous silicon. A linear relationship between the transmitted light intensity and the percentage of porosity was calculated using an FDTD model [114].

Barth et al. designed a hybrid nanophotonic device that can achieve metal nanoparticles nanoassembling in the cavity because metal nanoparticles localize themselves in positions with high electric field intensity, as shown in Fig. 11. FDTD was adopted to analyze the electric field in the designed cavity. FDTD simulation results showed that when a gold nanorod was inside the designed cavity, the electric field maximum moved from the cavity surface to the nanorod surface [122]. Lee and Hahn applied FDTD to obtain a localized field distribution on the photoresist under C-shaped and bowtie-shaped apertures during nanolithography. The calculated field distribution was used to predict the profile of the nanopatterns and optimize the initial parameters of nanolithography [123].

As the light transportation through the nanostructure can be simulated by FDTD, this function makes FDTD a candidate model for optimizing the parameters for controlling the nanolithography process, which can hardly be accessed by direct measurement methods. The FDTD method can

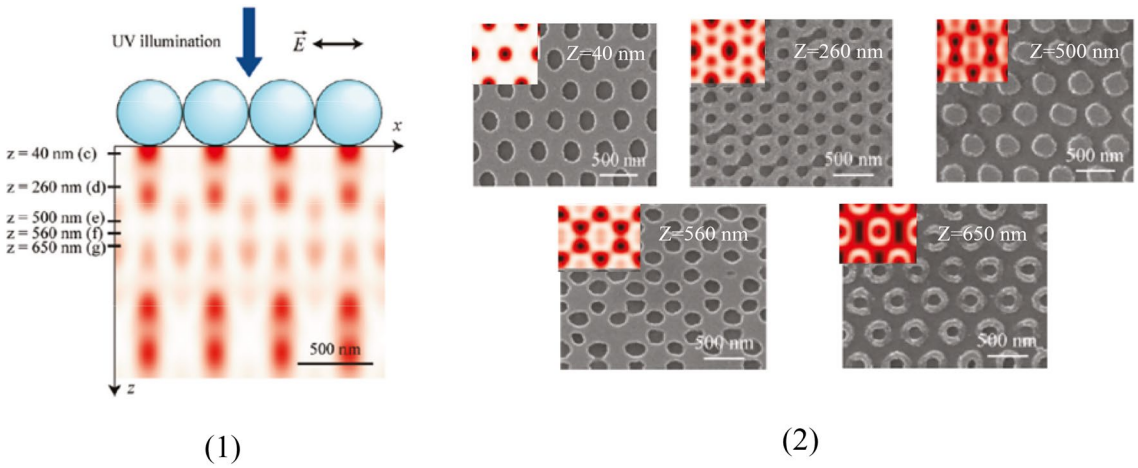

Fig. 10 Penetration depth in nanolithography. **1** Schematic of the nanolithography process. **2** SEM images of the fabricated structure versus depth from 40 to 650 nm [119]

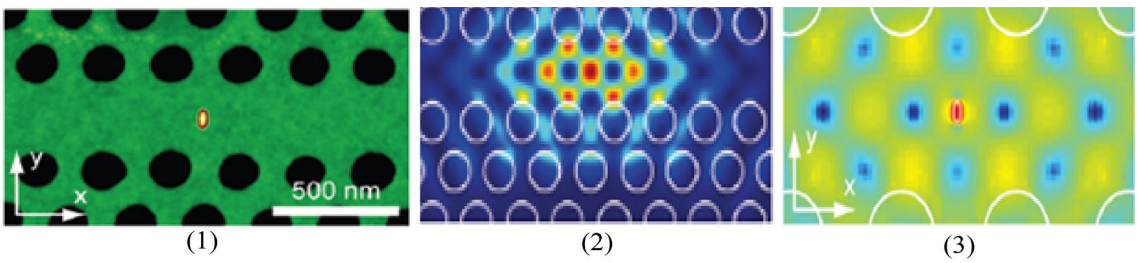

Fig. 11 Nanoparticle assembly process modeled by FDTD. **1** AFM image of a cavity with a gold nanorod. **2** Electric field distribution of a cavity without a gold nanorod. **3** Electric field distribution of a cavity with a gold nanorod [122]

also simulate the internal variation in the nanostructure. This capability makes it a powerful tool for understanding the physical variation inside the raw material. However, as one of the nanoscale modeling methods, FDTD shares the same problem as the MD method of a high computational load. The discrete spatial sections and time steps must be sufficiently small to satisfy the requirement of the Nyquist theorem. In addition, constrained by the core theories of electromagnetic waves, FDTD can only be applied in nanolithography or other procedures affected by microwave, UV, visible, or infrared light.

3.3 Monte Carlo Method (or Monte Carlo Molecular Method)

The MC method is a numerical approach to solving deterministic problems with random trials. It was first developed in the 1940s at Los Alamos National Laboratory [124]. In simulating molecule behavior in a complex macromolecular system, the method generates a molecular ensemble under specific thermodynamic conditions by assuming stochastic distribution in the molecule displacement [125]. Compared with the MD method, the MC method does not provide information about time evolution [126]. The rationality of updating the molecular configuration is determined by the molecular distribution probability variation and the resulting change in potential/dynamic energy. The MC method has been applied to studying heat conduction characteristics in nanostructures [127], gas absorption ratios of nanomaterial [128, 129], critical dimension formation during nanomanufacturing [130, 131], and cutting forces/temperatures in nanometric cutting processes [132].

3.3.1 Working Principle

The MC method assumes the number of particles, system volume, and temperature as constants in each thermodynamic system. Accordingly, it models the system ensemble as a representative of all molecular states [131]. The system ensemble is expressed as a function of the particle variables (position, momentum) and the material properties [132]:

$$\langle A\rangle = \frac{\int_{-\infty}^{+\infty} \exp(-\beta E(\vec{r}^N,\vec{p}^N))A(\vec{r}^N,\vec{p}^N)\mathrm{d}\vec{r}^N\mathrm{d}\vec{p}^N}{\int_{-\infty}^{+\infty} \exp(-\beta E(\vec{r}^N,\vec{p}^N))\mathrm{d}\vec{r}^N\mathrm{d}\vec{p}^N},\ \beta = \frac{1}{k_B T} \tag{6}$$

where k_B is Boltzmann's constant, T is the system temperature, $E(\vec{r}^N,\vec{p}^N)$ is the total potential energy of the N particles at position $\vec{r}^N$ with momentum $\vec{p}^N$($\vec{r}^N$ and $\vec{p}^N$ are N-dimensional arrays). $A(\vec{r}^N,\vec{p}^N)$ is a generic property representing the potential energy, kinetic energy, local density, coordination number, or radius of gyration. Because of the nonlinear terms in Eq. (6), the solution is generally approximated through numerical methods. In the system ensemble, the space is discretized into grid cells to calculate the behavior over the entire space. To reduce the computational load, the MC method adopts the metropolis acceptance criterion to determine the states. The metropolis acceptance criterion always accepts the state where the potential energy is smaller than the previous state. Otherwise, the system rejects the new state by following a certain probability that is determined by the Boltzmann distribution [126, 133, 134]:

$$\Pr(\vec{r}^N,\vec{p}^N) = \frac{\exp(-\beta H(\vec{r}^N,\vec{p}^N))}{\int \mathrm{d}p^N\mathrm{d}r^N \exp(-\beta H(\vec{r}^N,\vec{p}^N))} \tag{7}$$

where $H(\vec{r}^N,\vec{p}^N)$ is the Hamiltonian value of the system with position $\vec{r}^N$ and momenta $\vec{p}^N$, determined by Hamilton's equations. For each grid or molecule, if the molecule transfers from state m to state n, the mathematical expression of the metropolis acceptance criterion in the MC molecular modeling can be expressed as [133]:

$$p_{mn} = \begin{cases} \exp(-\beta(E(n)-E(m))) & E(n)-E(m) > 0 \\ 1 & E(n)-E(m) < 0 \end{cases} \tag{8}$$

where E is the potential energy of the particle. Based on the principle of the MC method, the ensemble in a specific thermodynamic condition can be calculated using the following iterative algorithm:

1. Select a particle randomly, and calculate the potential energy $E(m)$.
2. Add a random displacement to the selected particle:

$$\vec{r}(n) = \vec{r}(m) + \Delta \tag{9}$$

3. Calculate the new potential energy $E(n)$.
4. Determine the new particle to accept or reject by Eq. (8). If $\Delta E < 0$, the new particle is accepted; if $\Delta E > 0$, draw a random number γ on the interval (0,1) and accept the new particle when $\exp(-\beta\Delta E) > \gamma$.
5. If the new particle is accepted, the particle movement and potential energy calculation are based on the new particle; if the new particle is rejected, the system update is based on the old particle's position.

3.3.2 Applications of the MC Method in Nanomanufacturing

In nanomanufacturing, the MC method has been used to model or simulate thermodynamic systems. Platzgummer et al. developed a model to simulate the ion beam nanoimprinting process [130]. The developed model included an MC module that simulated sputter yield under different ion beam angles [130]. Tang et al. studied the heat of a nanofilm based on the MC method [135]. Physically, the

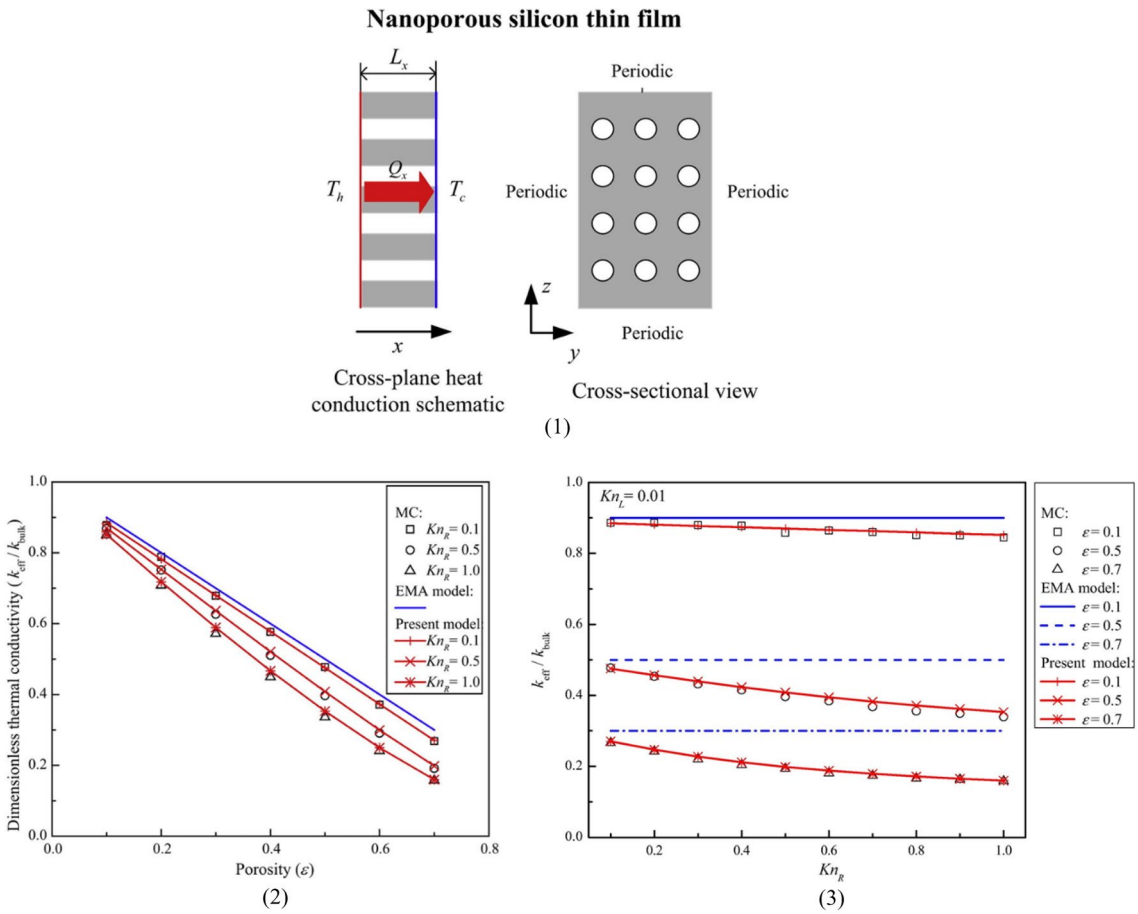

Fig. 12 Nanofilm thermal conductivity modeled with the MC method. **1** Schematic for cross-plane heat conduction in nanoporous silicon film. **2** Thermal conductivity of nanoporous film versus pore radius (Kn_R: pore radius; k_{eff}/k_{bulk}: effective thermal conductivity). **3** Thermal conductivity of nanoporous film at different porosity levels (ε: porosity) [127]

system heats one side of the nanofilm with a laser beam and measures the temperature difference across the film, as shown in Fig. 12 (1) [127]. The simulation reveals that the porosity, film thickness, and pore radius codetermine the thermal conductivity, as shown in Figs. 12 (2, 3). The simulation results also indicate that the MC method estimates the thermal conductivity more accurately than the conventional effective medium approach model in reference to the experimental results [127]. Leila compared the MC method and Langevin dynamic simulation in a study of SnO_2 nanofilm absorbance when it is used as a sensor to detect ethanol [127]. The data show that the two models produce consistent results in simulating the sensing process [129].

Komanduri et al. studied the local temperate in the cutting zone of the nanometric cutting process based on the MC method and compared the computational load with that of the MD method, as shown in Figs. 13 (1, 2) [133]. Figure 13 (1) shows that when the number of atoms increases, the difference in computation time between MD and MC increases exponentially. The relationship is observed when the cutting velocity is under 500 m/s, as seen in Fig. 13 (2) [133]. Zhu et al. built a semiempirical model based on density functional theory combined with the MC method to study the relationship between the catalyst particle and the carbon nanotube diameters and compared the results with that from the MD model [131, 136]. A good agreement was shown between the results of the two models.

According to the literature, MC can be used to simulate thermodynamic systems. As the MC method considers state transitions instead of continuous time steps, it only discretizes the space or volume of the object. As a result, the computational load is lighter than that of the MD and FDTD methods. However, the principle of the MC method also determines that the dynamics in the time domain cannot be provided in the results [134].

3.4 Finite Element Method

Finite element (FE) analysis is a numerical method for solving continuum mechanics problems by dividing a continuous

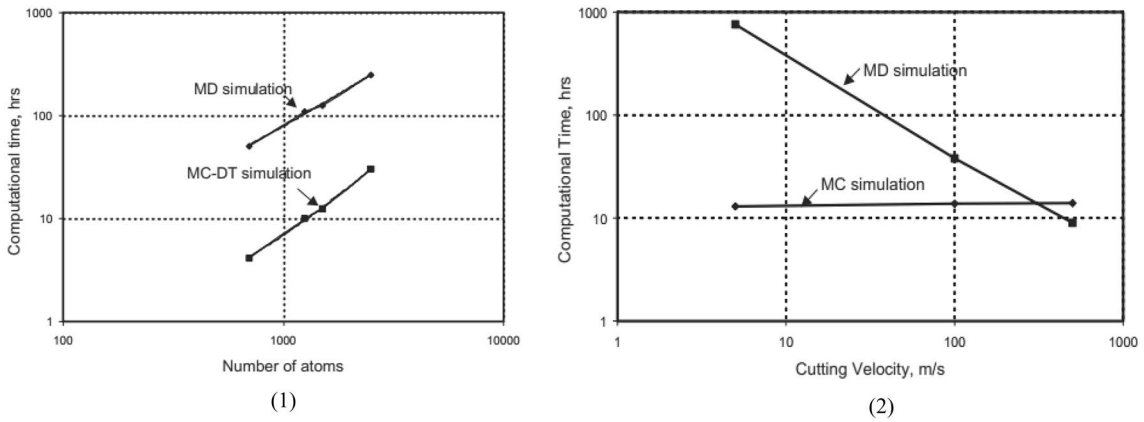

Fig. 13 Computational time comparison between the MC and MD methods [133]

structure into a finite number of structural elements. The conventional FE method assumes a linear relationship among the elements, thereby transforming a nonlinear problem into a multi-degree-of-freedom linear problem [137, 138]. Over the last 20 years, the FE method has been applied in nanomanufacturing to model nanostructures. As the FE method (FEM) does not need to model each molecule, as in the MD, FDTD, or MC methods, the meshed element only needs to satisfy the dimensional requirement of the specific nanostructure. Consequentially, the computational load of the FE method is generally much lower than that of the other methods. The FEM has been used to calculate the interfacial adhesion on top of nanofilms [139], the stiffness tensor of nanocomposite material [140], the tomography of nanostructure [141], the tensile modulus [142], and the cutting force during the nanometric cutting process [143].

Figure 14 shows a study of the interfacial adhesive characteristic of nanofilm deposited on a Cu/Si substrate using FE analysis and experiments [139]. The FE model simulated the process of a tool indenting and scratching the surface of the nanofilm and accordingly determined the critical force for different nanofilm thicknesses, as shown in Fig. 14 (1). The results show good agreement between the experimental and FE simulation results [Fig. 14 (2)]. Li et al. modeled silicon nanofilms decorated with nanopillar arrays to calculate the light absorbance of the nanofilms [144]. The simulation results were verified via the transfer matrix method [145], as shown in Fig. 15 (1, 2). The difference between the results from the two methods is shown to be below 0.25%. Liu et al. simulated the nanoimprinting process with the FE method on the ABAQUS platform and validated the results experimentally [146]. The simulation model achieves an error of 8.3% in the ratio of formation height to mold depth relative to the experimental data [141].

Sun and Cheng presented a combined FE–MD model to simulate crystal aluminum processed by nanometric cutting [143, 147]. The developed simulation model employs the MD method to model the cutting zone on the nanometer

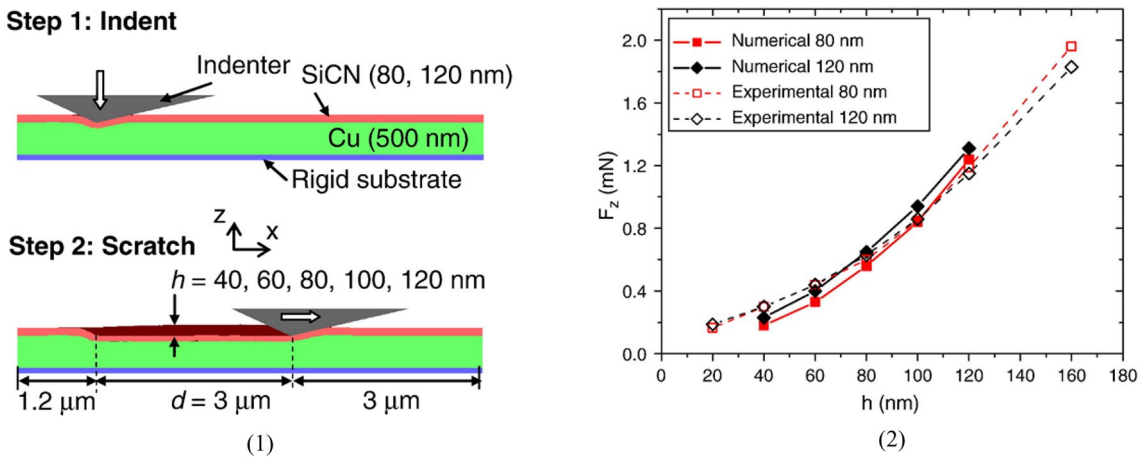

Fig. 14 Nanofilm scratching modeled based on the FE method. **1** Setup of a nanoscratch on the nanofilm. **2** Comparison of experimental and FEM results with 80-nm and 120-nm film thicknesses (h: penetrations of indenter; F_z: critical force) [139]

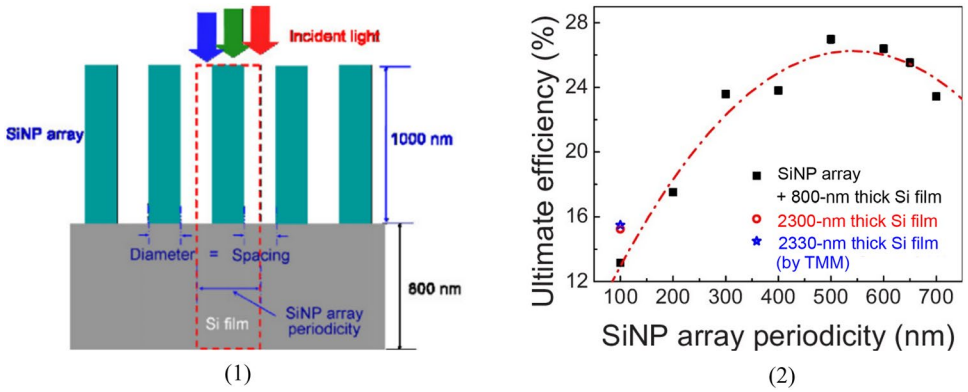

Fig. 15 Nanofilm with pillar array modeled in FE software. **1** Schematic of light incident into nanofilm decorated by nanopillars. **2** Efficiency function with array periodicity with exact values of 2330-nm film calculated by TMM and FEM [144]

scale and then uses the FE method to model the rest of the workpiece to reduce the computational load while maintaining the accuracy, as shown in Fig. 16 [143]. Liu and Jiang developed an atomic-scale FE (AFE) method in which the atoms of the processed material are modeled as nodes for calculating the process parameters, such as displacement, strain, stress, and temperature [146]. The CPU time and the number of iterations required for the developed method were compared with those of the MD method. The CPU time for calculating 3200 atoms by the AFE method is 65 s in 31 iterations and 4000 s by the MD method in 9000 iterations, which indicates that AFE reduces the computation time approximately 60-fold [148].

4 Discussion

Compared to direct measurement methods, such as AFM and EBM, indirect measurement methods, particularly the data-based methods, are advanced in fast response to estimate the CDs from the measured process variables. Although training a data-based model can take hours, using the trained model to estimate the CDs takes less than a second [53]. The physics-based methods generally have a longer response time than data-based methods because of the heavy computational load to simulate the behavior of particles or structures on the nanoscale. The actual processing time depends on the scale of the simulation in specific applications. Table 3 summarizes the four physics-based modeling methods in terms of computational efficiency, application, and limitation. Because of the constraint of the working principles, the FDTD method is generally adopted in an application involving microwaves, such as nanolithography and polarization processes. The MC method is advanced in simulating thermodynamics without considering each time step. The MD and FE methods are universal tools for modeling most nanomanufacturing processes. The selection and application of these physics-based models can be determined by the nature of the manufacturing process and the available computational capability [81]. All physics-based methods take seconds to hours to finish simulating a model. Although they can hardly be used for online control based on the present computational hardware, the simulated chemical reactions and physical behavior of the particles provide a theoretical basis for indirect measurement.

Uncertainty is an essential characteristic that quantifies the reliability of measurement results. In the direct measurement methods, a measurement result is determined by the

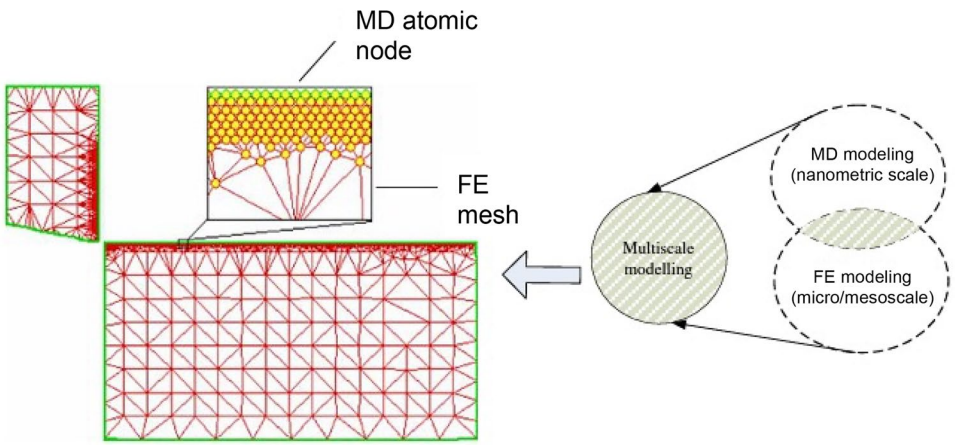

Fig. 16 Multiscale simulation model of the nanomatrix cutting process [143]

Table 3 Computational efficiency and application of physics-based methods

Modeling method	Modeling dimension	Computational efficiency	Application	Limitation
MD	$<50\times50\times50$ nm^3 [85, 107]	100 h for 1000 atoms [133]	Nanotensile, nanoscratch, nanometric cutting, depositing, assemble, adsorption analysis	Large computational load
MC	~120 nm [135]	~8 h for 1000 atoms [133]	Thermal conduction, nanometric cutting, adsorption analysis, nanoimprinting	Cannot study process, structure perturbations
FDTD	$\sim100\times100\times100$ nm^3 [123]	140 Mcells/s [155], 10 h [135]	Nanolithography, plasmon polariton	Application limited
FE	6000×600 nm^3 [139]	65 s for 3200 atoms [148]	Nanometric cutting, nanoscratch, nanotensile, nanoimprinting	Microscale simulation

physical structure of the probes or light/X-ray beams, and the uncertainty is closely related to the system hardware. In comparison, the uncertainty associated with the indirect methods can result from the following four factors [48, 62, 63, 77, 78, 118–130, 149–151]:

(1) The physical limitation of the instrument used when measuring process variables associated with the nanomanufacturing process;
(2) Simplifications and assumptions made when interpreting the measured parameters using empirical or regression models;
(3) The disturbance experienced during the measurement process, such as noise, environmental conditions, and electromagnetic pulses;
(4) Variation in the execution of the instrument operator when performing the measurement.

Because indirect measurement methods use the ground truth provided by direct measurement methods for model training, calibration, and validation, the uncertainty of the direct measurement method will be incorporated into the outcome of the indirect methods. As a result, indirect methods may have a higher level of uncertainty and a lower level of accuracy than direct methods.

Table 4 summarizes the validation methods in the literature. The AFM and SEM methods are most used to establish the ground truth of the CDs of nanostructures because of their high accuracy in quantifying the dimensional measurement and good adaptability to work with different types of nanostructures, such as fins, channels, films, and tubes.

5 Conclusions

This paper reviewed indirect measurement methods for monitoring the nanomanufacturing process and measuring the properties of nanoscale products. Compared with direct measurement methods, such as AFM, SEM, PiFM, and EFM, which use probes or electron/light beams to measure the geometry of nanostructures, indirect measurement methods exploit measuring the CDs in situ without interfering with the manufacturing process. This paper categorizes the indirect measurement methods into two major classes: data-based and physics-based methods. The data-based methods establish the relationship between in-process parameters and properties of the nanostructures through machine learning models. These machine learning models are trained by historical data from experimental studies and provide high accuracy when much data are collected from various conditions. The physics-based modeling method, in comparison, depends on the underlying physics of the manufacturing process to establish the process–property correlation. The numerical models in the physics-based modeling method can simulate the physical or chemical dynamics during the nanomanufacturing

Table 4 Validation of indirect measurement methods

Indirect methods		Validation method (direct)			
Data-based		AFM [78, 149, 151]	SEM [48, 77, 151, 154]	OSM [64]	
Physics-based	MD				TEM [106, 108, 110]
	MC		SEM [130]		
	FDTD	AFM [118]	SEM [56, 118, 119]		
	FE		SEM [139, 141]		

process, allowing accurate predictions to be provided with limited historical data. However, the computational load of the numerical simulation quickly increases with increasing model complexity and spatial resolution. As the indirect methods infer the CDs of nanoproducts from the in-process parameters accessible by the sensors during the nanomanufacturing process, they can predict the nanoproduct quality and provide feedback to fine-tune the control parameters in nanomanufacturing. In recent years, indirect methods have received increased attention due to the increased demand for real-time control for improved accuracy and stability in nanomanufacturing. Questions such as how to build computational data-based models with improved accuracy, how to fully understand the physics of the nanomanufacturing process, and how to combine the physics- and data-based models to address the generality and accuracy are still major challenges that require further research.

Declarations

Conflict of interest The authors have no conflicts of interest to declare that are relevant to the content of this article.

References

1. Fang FZ, Zhang XD, Gao W, Guo YB, Byrne G, Hansen HN (2017) Nanomanufacturing—perspective and applications. CIRP Ann 66:683–705. https://doi.org/10.1016/j.cirp.2017.05.004
2. Mukhtar M, Pillai U (2015) Nanomanufacturing: application of nanotechnology in manufacturing industries. Nanotechnol Law Bus 12:5–18
3. Kurata S, Hayashi K, Ishikawa A, Kondo M (2001) Integrated thin-film solar battery and method of manufacturing the same. U.S. Patent 6,265,652.
4. Wang Y, Chen J, Chen L, Chen YB, Wu LM (2010) Shape-controlled solventless syntheses of nano Bi disks and spheres. Cryst Growth Des 10:1578–1584. https://doi.org/10.1021/cg9010949
5. Wernik JM, Meguid SA (2011) Multiscale modeling of the nonlinear response of nano-reinforced polymers. Acta Mech 217:1–16. https://doi.org/10.1007/s00707-010-0377-7
6. Zhang Z, Yuan Y, Fang Y, Liang L, Ding H, Jin L (2007) Preparation of photocatalytic nano-ZnO/TiO2 film and application for determination of chemical oxygen demand. Talanta 73:523–528. https://doi.org/10.1016/j.talanta.2007.04.011
7. Jin Z, Zhou HJ, Jin ZL, Savinell RF, Liu CC (1998) Application of nano-crystalline porous tin oxide thin film for CO sensing. Sens Actuators, B Chem 52:188–194. https://doi.org/10.1016/S0925-4005(98)00272-X
8. Sun W, Qin P, Gao H, Li G, Jiao K (2010) Electrochemical DNA biosensor based on chitosan/nano-V2O5/MWCNTs composite film modified carbon ionic liquid electrode and its application to the LAMP product of *Yersinia enterocolitica* gene sequence. Biosens Bioelectron 25:1264–1270. https://doi.org/10.1016/j.bios.2009.10.011
9. Zhou H, Chen H, Luo S, Chen J, Wei W, Kuang Y (2005) Glucose biosensor based on platinum microparticles dispersed in nano-fibrous polyaniline. Biosens Bioelectron 20:1305–1311. https://doi.org/10.1016/j.bios.2004.04.024
10. Chang S, Geng Y, Yan Y (2021) Tip-based nanomachining on thin films: a mini review. Nanomanuf Metrol 5:2–22. https://doi.org/10.1007/s41871-021-00115-5
11. Deshwal D, Narwal AK (2021) An extensive review of nanotubes-based mass sensors. J Micro Nano-Manuf 9:020801-1–20808. https://doi.org/10.1115/1.4051261
12. Zhu D, Chen YL, Miller RA (2003) Defect clustering and nano-phase structure characterization of multicomponent rare earth-oxide-doped zirconia-yttria thermal barrier coatings. In: 27th annual cocoa beach conference on advanced ceramics and composites: a: ceramic engineering and science proceedings 24: 469–475. https://doi.org/10.1002/9780470294802.ch75
13. Wang Z, Han E, Ke W (2007) Fire-resistant effect of nanoclay on intumescent nanocomposite coatings. J Appl Polym Sci 103:1681–1689. https://doi.org/10.1002/app.25096
14. Liu K, Jiang L (2012) Bio-inspired self-cleaning surfaces. Annu Rev Mater Res 42:231–263. https://doi.org/10.1146/annurev-matsci-070511-155046
15. Wu D, Long M (2011) Realizing visible-light-induced self-cleaning property of cotton through coating N-TiO2 film and loading AgI particles. ACS Appl Mater Interfaces 3:4770–4774. https://doi.org/10.1021/am201251d
16. Gojny FH, Wichmann MHG, Fiedler B, Schulte K (2005) Influence of different carbon nanotubes on the mechanical properties of epoxy matrix composites–a comparative study. Compos Sci Technol 65:2300–2313. https://doi.org/10.1016/j.compscitech.2005.04.021
17. Ullbrand JM, Córdoba JM, Tamayo-Ariztondo J, Elizalde MR, Nygren M, Molina-Aldareguia JM, Odén M (2010) Thermo-mechanical properties of copper–carbon nanofibre composites prepared by spark plasma sintering and hot pressing. Compos Sci Technol 70:2263–2268. https://doi.org/10.1016/j.compscitech.2010.08.016
18. Daoush WM, Lim BK, Mo CB, Nam DH, Hong SH (2009) Electrical and mechanical properties of carbon nanotube reinforced copper nanocomposites fabricated by electroless deposition process. Mater Sci Eng, A 513:247–253. https://doi.org/10.1016/j.msea.2009.01.073
19. Shimizu Y, Miki S, Soga T, Itoh I, Todoroki H, Hosono T, Sakaki K et al (2008) Multi-walled carbon nanotube-reinforced magnesium alloy composites. Scripta Mater 58:267–270. https://doi.org/10.1016/j.scriptamat.2007.10.014
20. Li Q, Viereckl A, Rottmair CA, Singer RF (2009) Improved processing of carbon nanotube/magnesium alloy composites. Compos Sci Technol 69:1193–1199. https://doi.org/10.1016/j.compscitech.2009.02.020
21. Xu FF, Fang FZ (2019) Micro-and Nano-Manufacturing. In: Handbook of manufacturing, pp 465–509.
22. O'Toole L, Kang C, Fang F (2020) Advances in rotary ultrasonic-assisted machining. Nanomanuf Metrol 3:1–25. https://doi.org/10.1007/s41871-019-00053-3

23. Hussain D, Ahmad K, Song J, Xie H (2016) Advances in the atomic force microscopy for critical dimension metrology. Meas Sci Technol 28:012001. https://doi.org/10.1088/0957-0233/28/1/012001
24. Dai G, Häßler-Grohne W, Hüser D, Wolff H, Danzebrink HU, Koenders L, Bosse H (2011) Development of a 3D-AFM for true 3D measurements of nanostructures. Meas Sci Technol 22:094009. https://doi.org/10.1088/0957-0233/22/9/094009
25. Misumi I, Kizu R, Itoh H, Kumagai K, Kobayashi K, Sigehuzi T (2021) Research activities of nanodimensional standards using atomic force microscopes, transmission electron microscope, and scanning electron microscope at the national metrology institute of Japan. Nanomanuf Metrol. https://doi.org/10.1007/s41871-021-00119-1
26. Dai G, Hahm K, Sebastian L, Heidelmann M (2022) Comparison of EUV photomask metrology between CD-AFM and TEM. Nanomanuf Metrol. https://doi.org/10.1007/s41871-022-00124-y
27. Delvallée A, Feltin N, Ducourtieux S, Trabelsi M, Hochepied JF (2015) Direct comparison of AFM and SEM measurements on the same set of nanoparticles. Meas Sci Technol 26:085601. https://doi.org/10.1088/0957-0233/26/8/085601
28. Murdick RA, Morrison W, Nowak D, Albrecht TR, Jahng J, Park S (2017) Photoinduced force microscopy: a technique for hyperspectral nanochemical mapping. Jpn J Appl Phys 56:08LA04. https://doi.org/10.7567/JJAP.56.08LA04
29. Jia Z, Hosobuchi K, Ito S, Shimizu Y, Gao W (2014) An improved scan mode in an electrostatic force microscope for surface profile measurement of micro-optics. J Adv Mech Design Syst Manuf. https://doi.org/10.1299/jamdsm.2014jamdsm0051
30. Li WL, Tao NR, Lu K (2008) Fabrication of a gradient nano-micro-structured surface layer on bulk copper by means of a surface mechanical grinding treatment. Scripta Mater 59:546–549. https://doi.org/10.1016/j.scriptamat.2008.05.003
31. Arslan I, Yates TJV, Browning ND, Midgley PA (2005) Embedded nanostructures revealed in three dimensions. Science 309:2195–2198. https://doi.org/10.1126/science.1116745
32. Van Aert S, Batenburg KJ, Rossell MD, Erni R, Tendeloo GV (2011) Three-dimensional atomic imaging of crystalline nanoparticles. Nature 470:374–377. https://doi.org/10.1038/nature09741
33. Attota R (2011) TSOM method for nanoelectronics dimensional metrology. AIP Conf Proc 1395:57–63. https://doi.org/10.1063/1.3657866
34. Bechtel HA, Muller EA, Olmon RL, Martin MC, Raschke MB (2014) Ultrabroadband infrared nanospectroscopic imaging. Proc Natl Acad Sci 111:7191–7196. https://doi.org/10.1073/pnas.1400502111
35. Huth F, Schnell M, Wittborn J, Ocelic N, Hillenbrand R (2011) Infrared-spectroscopic nanoimaging with a thermal source. Nat Mater 10:352–356. https://doi.org/10.1038/nmat3006
36. Chao W, Harteneck BD, Liddle JA, Anderson EH, Attwood DT (2005) Soft X-ray microscopy at a spatial resolution better than 15 nm. Nature 435:1210–1213. https://doi.org/10.1038/nature03719
37. Griffiths PR (2009) Infrared and Raman instrumentation for mapping and imaging. Imaging Infrared Raman Spectrosc. https://doi.org/10.1002/9783527628230
38. Hollricher O (2010) Raman instrumentation for confocal Raman microscopy. Confocal Raman microscopy. Springer, Berlin. pp 43–60. https://doi.org/10.1007/978-3-642-12522-5_3
39. Tougaard S (2010) Energy loss in XPS: Fundamental processes and applications for quantification, non-destructive depth profiling and 3D imaging. J Electron Spectrosc Relat Phenom 178:128–153. https://doi.org/10.1016/j.elspec.2009.08.005
40. Panas RM, Cuadra JA, Mohan KA, Morales RE (2021) A systems approach to estimating the uncertainty limits of X-ray radiographic metrology. J Micro Nano-Manuf 9:010901. https://doi.org/10.1115/1.4049421
41. Prats-Mateu B, Gierlinger N (2017) Tip in–light on: Advantages, challenges, and applications of combining AFM and Raman microscopy on biological samples. Microsc Res Tech 80:30–40. https://doi.org/10.1002/jemt.22744
42. Asano M, Yoshikawa R, Hirano T, Abe H, Matsuki K, Tsuda H, Komori M, Ojima T, Yonemitsu H, Kawamoto A (2017) Metrology and inspection required for next-generation lithography. Jpn J Appl Phys 56:06GA01. https://doi.org/10.7567/JJAP.56.06GA01
43. Hauser M, Wojcik M, Kim D, Mahmoudi M, Li W, Xu K (2017) Correlative super-resolution microscopy: new dimensions and new opportunities. Chem Rev 117:7428–7456. https://doi.org/10.1021/acs.chemrev.6b00604
44. Abou-Ras D (2017) Correlative microscopy analyses of thin-film solar cells at multiple scales. Mater Sci Semicond Process 65:35–43. https://doi.org/10.1016/j.mssp.2016.07.009
45. Jang YS, Kim SW (2018) Distance measurements using mode-locked lasers: a review. Nanomanuf Metrol 1:131–147. https://doi.org/10.1007/s41871-018-0017-8
46. Nguyen CV, So C, Stevens RM, Li Y, Delziet L, Sarrazin P, Meyyappan M (2004) High lateral resolution imaging with sharpened tip of multi-walled carbon nanotube scanning probe. J Phys Chem B 108:2816–2821. https://doi.org/10.1021/jp0361529
47. Ahn T, Oh S, Hu X, Lee JW, Park CW, Yang HM, Kim CG, Kim JD (2014) Controlled self-assembly for high-resolution magnetic printing. Small 10:1081–1085. https://doi.org/10.1002/smll.201301983
48. Chen PH, Yau C, Wu KY, Lin S, Shih HC (2005) Application of the Taguchi's design of experiments to optimize a bromine chemistry-based etching recipe for deep silicon trenches. Microelectron Eng 77:110–115. https://doi.org/10.1016/j.mee.2004.09.001
49. Azhari AW, Sopian K, Desa MKM, Zaidi SH (2015) Optimization of silver-assisted nano-pillar etching process in silicon. Appl Surf Sci 357:1863–1877. https://doi.org/10.1016/j.apsusc.2015.09.088
50. Tsujino K, Matsumura M (2007) Morphology of nanoholes formed in silicon by wet etching in solutions containing HF and H2O2 at different concentrations using silver nanoparticles as catalysts. Electrochim Acta 53:28–34. https://doi.org/10.1016/j.electacta.2007.01.035
51. Yördem OS, Papila M, Menceloğlu YZ (2008) Effects of electrospinning parameters on polyacrylonitrile nanofiber diameter: An investigation by response surface methodology. Mater Des 29:34–44. https://doi.org/10.1016/j.matdes.2006.12.013
52. Lu JC, Jeng SL, Wang K (2009) A review of statistical methods for quality improvement and control in nanotechnology. J Qual Technol 41:148–164. https://doi.org/10.1080/00224065.2009.11917770
53. Zhang H, Chung SW, Mirkin CA (2003) Fabrication of sub-50-nm solid-state nanostructures on the basis of dip-pen nanolithography. Nano Lett 3:43–45. https://doi.org/10.1021/nl025847 3
54. Ng CK, Melkote SN, Rahman M, Kumar AS (2006) Experimental study of micro-and nano-scale cutting of aluminum 7075–T6. Int J Mach Tools Manuf 46:929–936. https://doi.org/10.1016/j.ijmachtools.2005.08.004
55. Zhang J (2014) Micro/Nano machining of steel and tungsten carbide utilizing elliptical vibration cutting technology. Dissertation, Nagoya University.

56. Uppuluri SMV, Kinzel EC, Li Y, Xu X (2010) Parallel optical nanolithography using nanoscale bowtie aperture array. Optics xpress 18:7369–7375. https://doi.org/10.1364/OE.18.007369
57. Piner RD, Zhu J, Xu F, Hong S, Mirkin CA (1999) "Dip-pen" nanolithography. Science 283:661–663. https://doi.org/10.1126/science.283.5402.661
58. Wilson P, Lekakou C, Watts JF (2013) In-plane conduction characterisation and charge transport model of DMSO co-doped, inkjet printed poly (3, 4-ethylenedioxythiophene): polystyrene sulfonate (PEDOT: PSS). Org Electron 14:3277–3285. https://doi.org/10.1016/j.orgel.2013.09.025
59. Kato Y, Adachi S (2012) Fabrication and optical characterization of Si nanowires formed by catalytic chemical etching in Ag2O/HF solution. Appl Surf Sci 258:5689–5697. https://doi.org/10.1016/j.apsusc.2012.02.063
60. Zhao F, Cheng GA, Zheng RT, Xia LY (2008) Effect of the microstructure of Ag catalysts in the fabricating process of silicon nanowires. J Korean Phys Soc 52:104–107. https://doi.org/10.3938/jkps.52.104
61. Xie WQ, Oh JI, Shen WZ (2011) Realization of effective light trapping and omnidirectional antireflection in smooth surface silicon nanowire arrays. Nanotechnology 22:065704. https://doi.org/10.1088/0957-4484/22/6/065704
62. Kotsiantis SB, Zaharakis I, Pintelas P (2007) Supervised machine learning: A review of classification techniques. Emerging Artif Intell Appl Comput Eng 160:3–24
63. Hou TH, Su CH, Liu WL (2007) Parameters optimization of a nano-particle wet milling process using the Taguchi method, response surface method and genetic algorithm. Powder Technol 173:153–162. https://doi.org/10.1016/j.powtec.2006.11.019
64. Dhall D, Kaur R, Juneja M (2019) Machine learning: a review of the algorithms and its applications. Proceedings of ICRIC 2019:47–63. https://doi.org/10.1007/978-3-030-29407-6_5
65. Ward L, Wolverton C (2017) Atomistic calculations and materials informatics: A review. Curr Opin Solid State Mater Sci 21:167–176. https://doi.org/10.1016/j.cossms.2016.07.002
66. Dimiduk DM, Holm EA, Niezgoda SR (2018) Perspectives on the impact of machine learning, deep learning, and artificial intelligence on materials, processes, and structures engineering. Integr Mater Manufact Innov 7:157–172. https://doi.org/10.1007/s40192-018-0117-8
67. Timoshenko J, Lu D, Lin Y, Frenkel AI (2017) Supervised machine-learning-based determination of three-dimensional structure of metallic nanoparticles. J Phys Chem Lett 8:5091–5098. https://doi.org/10.1021/acs.jpclett.7b02364
68. Malola S, Nieminen P, Pihlajamäki A, Hämäläinen J, Kärkkäinen T, Häkkinen H (2019) A method for structure prediction of metal–ligand interfaces of hybrid nanoparticles. Nat Commun 10:1–10. https://doi.org/10.1038/s41467-019-12031-w
69. Yan X, Sedykh A, Wang W, Zhao X, Yan B, Zhu H (2019) In silico profiling nanoparticles: predictive nanomodeling using universal nanodescriptors and various machine learning approaches. Nanoscale 11:8352–8362. https://doi.org/10.1039/C9NR00844F
70. Parker AJ, Barnard AS (2019) Selecting appropriate clustering methods for materials science applications of machine learning. Adv Theory Simul 2:1900145. https://doi.org/10.1002/adts.201900145
71. Kiarashinejad Y, Abdollahramezani S, Adibi A (2020) Deep learning approach based on dimensionality reduction for designing electromagnetic nanostructures. NPJ Comput Mater 6:1–12. https://doi.org/10.1038/s41524-020-0276-y
72. Barnard AS, Opletal G (2020) Selecting machine learning models for metallic nanoparticles. Nano Futur 4:035003. https://doi.org/10.1088/2399-1984/ab9c3b
73. Boulogeorgos AAA, Trevlakis SE, Tegos SA, Papanikolaou VK, Karagiannidis GK (2020) Machine learning in nano-scale biomedical engineering. IEEE Trans Molecular, Biol Multi-Scale Commun 7:10–39. https://doi.org/10.1109/TMBMC.2020.3035383
74. Brown KA, Brittman S, Maccaferri N, Jariwala D, Celano U (2019) Machine learning in nanoscience: big data at small scales. Nano Lett 20:2–10. https://doi.org/10.1021/acs.nanolett.9b04090
75. Müller P, Abuhattum S, Möllmert S, Ulbricht E, Taubenberger AV, Guck J (2019) Nanite: using machine learning to assess the quality of atomic force microscopy-enabled nanoindentation data. BMC Bioinf 20:1–9. https://doi.org/10.1186/s12859-019-3010-3
76. Erdemir F (2017) Study on particle size and X-ray peak area ratios in high energy ball milling and optimization of the milling parameters using response surface method. Measurement 112:53–60. https://doi.org/10.1016/j.measurement.2017.08.021
77. Hung CC, Lin HC, Shih HC (2002) Response surface methodology applied to silicon trench etching in Cl2/HBr/O2 using transformer coupled plasma technique. Solid-State Electron 46:791–795. https://doi.org/10.1016/S0038-1101(02)00004-7
78. Ting HT, Abou-El-Hossein K, Chua HB (2011) Predictive modelling of etching process of machinable glass ceramics, boron nitride, and silicon carbide. Mater Sci Appl 2:1601–1621. https://doi.org/10.4236/msa.2011.211214
79. Lin X, Si Z, Fu W, Yang J, Guo S, Cao Y, Zhang J, Wang X, Liu P, Jiang K, Zhao W (2018) Intelligent identification of two-dimensional nanostructures by machine-learning optical microscopy. Nano Res 11:6316–6324. https://doi.org/10.1007/s12274-018-2155-0
80. Du T, Liu H, Tang L, Sørensen SS, Bauchy M, Smedskjaer MM (2021) Predicting fracture propensity in amorphous alumina from its static structure using machine learning. ACS Nano 15:17705–17716. https://doi.org/10.1021/acsnano.1c05619
81. Gao R, Wang L, Teti R, Dornfeld D, Kumara S, Mori M, Helu M (2015) Cloud-enabled prognosis for manufacturing. CIRP Ann 64:749–772. https://doi.org/10.1016/j.cirp.2015.05.011
82. Vlachakis D, Bencurova E, Papangelopoulos N, Kossida S (2014) Current state-of-the-art molecular dynamics methods and applications. Adv Protein Chem Struct Biol 94:269–313. https://doi.org/10.1016/B978-0-12-800168-4.00007-X
83. Guo C, Luo Y, Zhou R, Wei G (2012) Probing the self-assembly mechanism of diphenylalanine-based peptide nanovesicles and nanotubes. ACS Nano 6:3907–3918. https://doi.org/10.1021/nn300015g
84. Wu B, Zhou J, Xue C, Liu H (2015) Molecular dynamics simulation of the deposition and annealing of NiAl film on Ni substrate. Appl Surf Sci 355:1145–1152. https://doi.org/10.1016/j.apsusc.2015.07.208
85. Lai M, Zhang X, Fang F, Wang Y, Feng M, Tian W (2013) Study on nanometric cutting of germanium by molecular dynamics simulation. Nanoscale Res Lett 8:1–10. https://doi.org/10.1186/1556-276X-8-13
86. Li C, Strachan A (2011) Effect of thickness on the thermomechanical response of free-standing thermoset nanofilms from molecular dynamics. Macromolecules 44:9448–9454. https://doi.org/10.1021/ma201927n
87. Monticelli L, Tieleman DP (2013) Force fields for classical molecular dynamics. Biomolecular Simul. https://doi.org/10.1007/978-1-62703-017-5_8
88. Van Westen T, Vlugt TJH, Gross J (2011) Determining force field parameters using a physically based equation of state. J Phys Chem B 115:7872–7880. https://doi.org/10.1021/jp2026219
89. Allinger NL (1977) Conformational analysis. 130. MM2. A hydrocarbon force field utilizing V1 and V2 torsional terms. J Am Chem Soc 99:8127–8134

90. Allinger NL, Yuh YH, Lii JH (1989) Molecular mechanics. The MM3 force field for hydrocarbons. 1. J Am Chem Soc 111:8551–8566. https://doi.org/10.1021/ja00205a001
91. Allinger NL, Chen K, Lii JH (1996) An improved force field (MM4) for saturated hydrocarbons. J Comput Chem 17:642–668. https://doi.org/10.1002/(SICI)1096-987X(199604)17:5/6<642::AID-JCC6>3.0.CO;2-U
92. González MA (2011) Force fields and molecular dynamics simulations. École thématique de la Société Française de la Neutronique 12:169–200. https://doi.org/10.1051/sfn/201112009
93. Cornell WD, Cieplak P, Bayly CI, Gould IR, Merz KM, Ferguson DM, Spellmeyer DC, Fox T, Caldwell JW, Kollman PA (1995) A second generation force field for the simulation of proteins, nucleic acids, and organic molecules. J Am Chem Soc 117:5179–5197. https://doi.org/10.1021/ja00124a002
94. MacKerell AD Jr, Bashford D, Bellott MLDR, Dunbrack RL Jr, Evanseck JD, Field MJ, Fischer S et al (1998) All-atom empirical potential for molecular modeling and dynamics studies of proteins. J Phys Chem B 102:3586–3616. https://doi.org/10.1021/jp973084f
95. Oostenbrink C, Villa A, Mark AE, Gunsteren WFV (2004) A biomolecular force field based on the free enthalpy of hydration and solvation: the GROMOS force-field parameter sets 53A5 and 53A6. J Comput Chem 25:1656–1676. https://doi.org/10.1002/jcc.20090
96. Jorgensen WL, Maxwell DS, Tirado-Rives J (1996) Development and testing of the OPLS all-atom force field on conformational energetics and properties of organic liquids. J Am Chem Soc 118:11225–11236. https://doi.org/10.1021/ja9621760
97. Sun H (1998) COMPASS: An ab initio force-field optimized for condensed-phase applications overview with details on alkane and benzene compounds. J Phys Chem B 102:7338–7364. https://doi.org/10.1021/jp980939v
98. Maple JR, Hwang MJ, Stockfisch TP, Dinur U, Waldman M, Ewig CS, Hagler AT (1994) Derivation of class II force fields. I. Methodology and quantum force field for the alkyl functional group and alkane molecules. J Comput Chem 15:162–182. https://doi.org/10.1002/jcc.540150207
99. Halgren TA (1996) Merck molecular force field. I. Basis, form, scope, parameterization, and performance of MMFF94. J Comput Chem 17:490–519. https://doi.org/10.1002/(SICI)1096-987X(199604)17:5/6%3c490::AID-JCC1%3e3.0.CO;2-P
100. Jorgensen WL, Tirado-Rives J (2005) Potential energy functions for atomic-level simulations of water and organic and biomolecular systems. Proc Natl Acad Sci 102:6665–6670. https://doi.org/10.1073/pnas.0408037102
101. Tuckerman M, Berne BJ, Martyna GJ (1992) Reversible multiple time scale molecular dynamics. J Chem Phys 97:1990–2001. https://doi.org/10.1063/1.463137
102. Peskin CS, Schlick T (1989) Molecular dynamics by the Backward-Euler method. Commun Pure Appl Math 42:1001–1031. https://doi.org/10.1002/cpa.3160420706
103. Memon SA, Ly DQ, Ahmed W (2017) Implementation of Crank-Nicolson scheme in cell dynamics simulation for diblock copolymers. Mater Today Proc 4:41–49. https://doi.org/10.1016/j.matpr.2017.01.191
104. Nakano A, Vashishta P, Kalia RK (1994) Massively parallel algorithms for computational nanoelectronics based on quantum molecular dynamics. Comput Phys Commun 83:181–196. https://doi.org/10.1016/0010-4655(94)90047-7
105. Meyer R (2014) Efficient parallelization of molecular dynamics simulations with short-ranged forces. J Phys Conf Ser 540:012006. https://doi.org/10.1088/1742-6596/540/1/012006
106. Tang DM, Ren CL, Wang MS, Wei X, Kawamoto N, Liu C, Bando Y, Mitome M, Fukata N, Golberg D (2012) Mechanical properties of Si nanowires as revealed by in situ transmission electron microscopy and molecular dynamics simulations. Nano Lett 12:1898–1904. https://doi.org/10.1021/nl204282y
107. Li Q, Huang C, Liang Y, Fu T, Peng T (2016) Molecular dynamics simulation of nanoindentation of Cu/Au thin films at different temperatures. J Nanomater. https://doi.org/10.1155/2016/9265948
108. Chen Y, Lin YC, Huang CW, Wang CW, Chen LJ, Wu WW, Huang Y (2012) Kinetic competition model and size-dependent phase selection in 1-D nanostructures. Nano Lett 12:3115–3120. https://doi.org/10.1021/nl300990q
109. Sindhu TK, Sarathi R, Chakravarthy SR (2007) Understanding nanoparticle formation by a wire explosion process through experimental and modelling studies. Nanotechnology 19:025703. https://doi.org/10.1088/0957-4484/19/02/025703
110. Xu Z, Yang X, Yang Z (2010) A molecular simulation probing of structure and interaction for supramolecular sodium dodecyl sulfate/single-wall carbon nanotube assemblies. Nano Lett 10:985–991. https://doi.org/10.1021/nl9041005
111. Yee K (1966) Numerical solution of initial boundary value problems involving Maxwell's equations in isotropic media. IEEE Trans Antennas Propag 14:302–307. https://doi.org/10.1109/TAP.1966.1138693
112. Umashankar K, Taflove A (1982) A novel method to analyze electromagnetic scattering of complex objects. IEEE Trans Electromagn Compat 4:397–405. https://doi.org/10.1109/TEMC.1982.304054
113. Shao DB, Chen SC (2005) Numerical simulation of surface-plasmon-assisted nanolithography. Opt Expr 13:6964–6973. https://doi.org/10.1364/OPEX.13.006964
114. Mishra CS, Palai G (2016) Manipulating light with porous silicon for investigation of porosity using finite difference time domain method. Optik 127:1195–1197. https://doi.org/10.1016/j.ijleo.2015.11.012
115. Jang JW, Park BC, Nettikadan S (2014) Generation of plasmonic Au nanostructures in the visible wavelength using two-dimensional parallel dip-pen nanolithography. Nanoscale 6:7912–7916. https://doi.org/10.1039/C4NR00568F
116. Yin Y, Xu S, Li T, Yin Y, Xia Y, Yin J (2017) 2D surface optical lattice formed by plasmon polaritons with application to nanometer-scale molecular deposition. Sci Rep 7:1–9. https://doi.org/10.1038/s41598-017-08175-8
117. Chew WC, Weedon WH (1994) A 3D perfectly matched medium from modified Maxwell's equations with stretched coordinates. Microw Opt Technol Lett 7:599–604. https://doi.org/10.1002/mop.4650071304
118. Wang L, Uppuluri SM, Jin EX, Xu X (2006) Nanolithography using high transmission nanoscale bowtie apertures. Nano Lett 6:361–364. https://doi.org/10.1021/nl052371p
119. Chang CH, Tian L, Hesse WR, Gao H, Choi HJ, Kim JG, Siddiqui M, Barbastathis G (2011) From two-dimensional colloidal self-assembly to three-dimensional nanolithography. Nano Lett 11:2533–2537. https://doi.org/10.1021/nl2011824
120. Kim Y, Jung H, Kim S, Jang J, Lee JY, Hahn JW (2011) Accurate near-field lithography modeling and quantitative mapping of the near-field distribution of a plasmonic nanoaperture in a metal. Opt Express 19:19296–19309. https://doi.org/10.1364/OE.19.019296
121. Amarie D, Rawlinson ND, Schaich WL, Dragnea B, Jacobson SC (2005) Three-dimensional mapping of the light intensity transmitted through nanoapertures. Nano Lett 5:1227–1230. https://doi.org/10.1021/nl050891e
122. Barth M, Schietinger S, Fischer S, Becker J, Nusse N, Aichele T, Lochel B, Sonnichsen C, Benson O (2010) Nanoassembled plasmonic-photonic hybrid cavity for tailored light-matter coupling. Nano Lett 10:891–895. https://doi.org/10.1021/nl903555u

123. Lee E, Hahn JW (2008) Modeling of three-dimensional photoresist profiles exposed by localized fields of high-transmission nano-apertures. Nanotechnology 19:275303. https://doi.org/10.1088/0957-4484/19/27/275303
124. Salvat F, Fernández-Varea JM, Acosta E, Sempau JP (2001) A code system for Monte Carlo simulation of electron and photon transport. Proceedings of a Workshop/Training Course, OECD/NEA, pp. 5–7.
125. Fichthorn KA, Weinberg WH (1991) Theoretical foundations of dynamical Monte Carlo simulations. J Chem Phys 95:1090–1096. https://doi.org/10.1063/1.461138
126. Paquet E, Viktor HL (2015) Molecular dynamics, Monte Carlo simulations, and Langevin dynamics: a computational review. Biomed Res Int. https://doi.org/10.1155/2015/183918
127. Hua YC, Cao BY (2017) Cross-plane heat conduction in nanoporous silicon thin films by phonon Boltzmann transport equation and Monte Carlo simulations. Appl Therm Eng 111:1401–1408. https://doi.org/10.1016/j.applthermaleng.2016.05.157
128. De Debiaggi SR, Crespo EA, Braschi FU, Bringa EM, Alí ML, Ruda M (2014) Hydrogen absorption in Pd thin-films. Int J Hydrogen Energy 39:8590–8595. https://doi.org/10.1016/j.ijhydene.2014.01.013
129. Mahdavian L (2012) Simulation of SnO2/WO3 nanofilms for alcohol of gas sensor based on metal dioxides: MC and LD studies. J Nanostruct Chem 3:1–9. https://doi.org/10.1186/2193-8865-3-1
130. Platzgummer E, Biedermann A, Langfischer H, Eder-Kapl S, Kuemmel M, Cernusca S, Loeschner H et al (2006) Simulation of ion beam direct structuring for 3D nanoimprint template fabrication. Microelectron Eng 83:936–939. https://doi.org/10.1016/j.mee.2006.01.140
131. Zhu W, Börjesson A, Bolton K (2010) DFT and tight binding Monte Carlo calculations related to single-walled carbon nanotube nucleation and growth. Carbon 48:470–478. https://doi.org/10.1016/j.carbon.2009.09.064
132. Metropolis N, Rosenbluth AW, Rosenbluth MN, Teller AH, Teller E (1953) Equation of state calculations by fast computing machines. J Chem Phys 21:1087–1092. https://doi.org/10.1063/1.1699114
133. Komanduri R, Narulkar R, Raff LM (2004) Monte Carlo simulation of nanometric cutting. Phil Mag 84:1155–1183. https://doi.org/10.1080/14786430310001646736
134. Earl DJ, Deem MW (2008) Monte Carlo simulations. Molecular modeling of proteins. Humana Press, Totowa, pp 25–36. https://doi.org/10.1007/978-1-59745-177-2_2
135. Tang DS, Hua YC, Cao BY (2016) Thermal wave propagation through nanofilms in ballistic-diffusive regime by Monte Carlo simulations. Int J Therm Sci 109:81–89. https://doi.org/10.1016/j.ijthermalsci.2016.05.030
136. Bolton K, Ding F, Rosén A (2006) Atomistic simulations of catalyzed carbon nanotube growth. J Nanosci Nanotechnol 6:1211–1224. https://doi.org/10.1166/jnn.2006.145
137. Hrennikoff A (1941) Solution of problems of elasticity by the framework method. J Appl Mech 8(4):A169–A175. https://doi.org/10.1115/1.4009129
138. Bhatti MA (2005) Fundamental finite element analysis and applications: with Mathematica and Matlab computations, Wiley, 2005. ISBN: 978-0-471-64808-6.
139. Roy S, Darque-Ceretti E, Felder E, Raynal F, Bispo I (2010) Experimental analysis and finite element modelling of nano-scratch test applied on 40–120 nm SiCN thin films deposited on Cu/Si substrate. Thin Solid Films 518:3859–3865. https://doi.org/10.1016/j.tsf.2010.02.004
140. Sheidaei A, Baniassadi M, Banu M, Askeland P, Pahlavanpour M, Kuuttila N, Pourboghrat F, Drzal LT, Garmestani H (2013) 3-D microstructure reconstruction of polymer nano-composite using FIB–SEM and statistical correlation function. Compos Sci Technol 80:47–54. https://doi.org/10.1016/j.compscitech.2013.03.001
141. Tsai CY, Lu YT, Sung CK, Chung CL (2010) Finite element method investigation into nanoimprinting of aluminum/polyimide bi-layer substrates. Microelectron Eng 87:2361–2367. https://doi.org/10.1016/j.mee.2010.04.009
142. Bhuiyan MA, Pucha RV, Worthy J, Karevan M, Kalaitzidou K (2013) Understanding the effect of CNT characteristics on the tensile modulus of CNT reinforced polypropylene using finite element analysis. Comput Mater Sci 79:368–376. https://doi.org/10.1016/j.commatsci.2013.06.046
143. Sun X, Cheng K (2010) Multi-scale simulation of the nanometric cutting process. Int J Adv Manuf Technol 47:891–901. https://doi.org/10.1007/s00170-009-2125-5
144. Li J, Yu HY, Wong SM, Zhang G, Sun X, Lo P, Kwong D (2009) Si nanopillar array optimization on Si thin films for solar energy harvesting. Appl Phys Lett 95:033102. https://doi.org/10.1063/1.3186046
145. Pendry JB (1994) Photonic band structures. J Mod Opt 41:209–229. https://doi.org/10.1080/09500349414550281
146. Liu B, Jiang H, Huang Y, Qu S, Yu MF, Hwang KC (2005) Atomic-scale finite element method in multiscale computation with applications to carbon nanotubes. Phys Rev B 72:035435. https://doi.org/10.1103/PhysRevB.72.035435
147. Komanduri R, Chandrasekaran N, Raff LM (2000) MD Simulation of nanometric cutting of single crystal aluminum–effect of crystal orientation and direction of cutting. Wear 242:60–88. https://doi.org/10.1016/S0043-1648(00)00389-6
148. Yakobson BI, Brabec CJ, Bernholc J (1996) Nanomechanics of carbon tubes: instabilities beyond linear response. Phys Rev Lett 76:2511. https://doi.org/10.1103/PhysRevLett.76.2511
149. Zhou W, Ding L, Yang S, Liu J (2011) Synthesis of high-density, large-diameter, and aligned single-walled carbon nanotubes by multiple-cycle growth methods. ACS Nano 5:3849–3857. https://doi.org/10.1021/nn200198b
150. Dhabak D, Pandit S (2011) Adaptive sampling algorithm for ANN-based performance modeling of nano-scale CMOS inverter. World Acad Sci Eng Technol 5:812–818. https://doi.org/10.5281/zenodo.1073529
151. Hong SW, Banks T, Rogers JA (2010) Improved density in aligned arrays of single-walled carbon nanotubes by sequential chemical vapor deposition on quartz. Adv Mater 22:1826–1830. https://doi.org/10.1002/adma.200903238
152. Botti S, Rufoloni A, Laurenzi S, Gay S, Rindzevicius T, Schmidt MS, Santonicola MG (2016) DNA self-assembly on graphene surface studied by SERS mapping. Carbon 109:363–372. https://doi.org/10.1016/j.carbon.2016.07.069
153. Jana NR, Gearheart L, Murphy CJ (2001) Wet chemical synthesis of high aspect ratio cylindrical gold nanorods. J Phys Chem B 105:4065–4067. https://doi.org/10.1021/jp0107964
154. Kim SH, Jeong C (2021) Feasibility of machine learning algorithms for predicting the deformation of anodic titanium films by modulating anodization processes. Materials 14:1089. https://doi.org/10.3390/ma14051089
155. Shams R, Sadeghi P (2011) On optimization of finite-difference time-domain (FDTD) computation on heterogeneous and GPU clusters. J Parallel Distrib Comput 71:584–593. https://doi.org/10.1016/j.jpdc.2010.10.011